RADIALcvt prototype design, simulation and testing

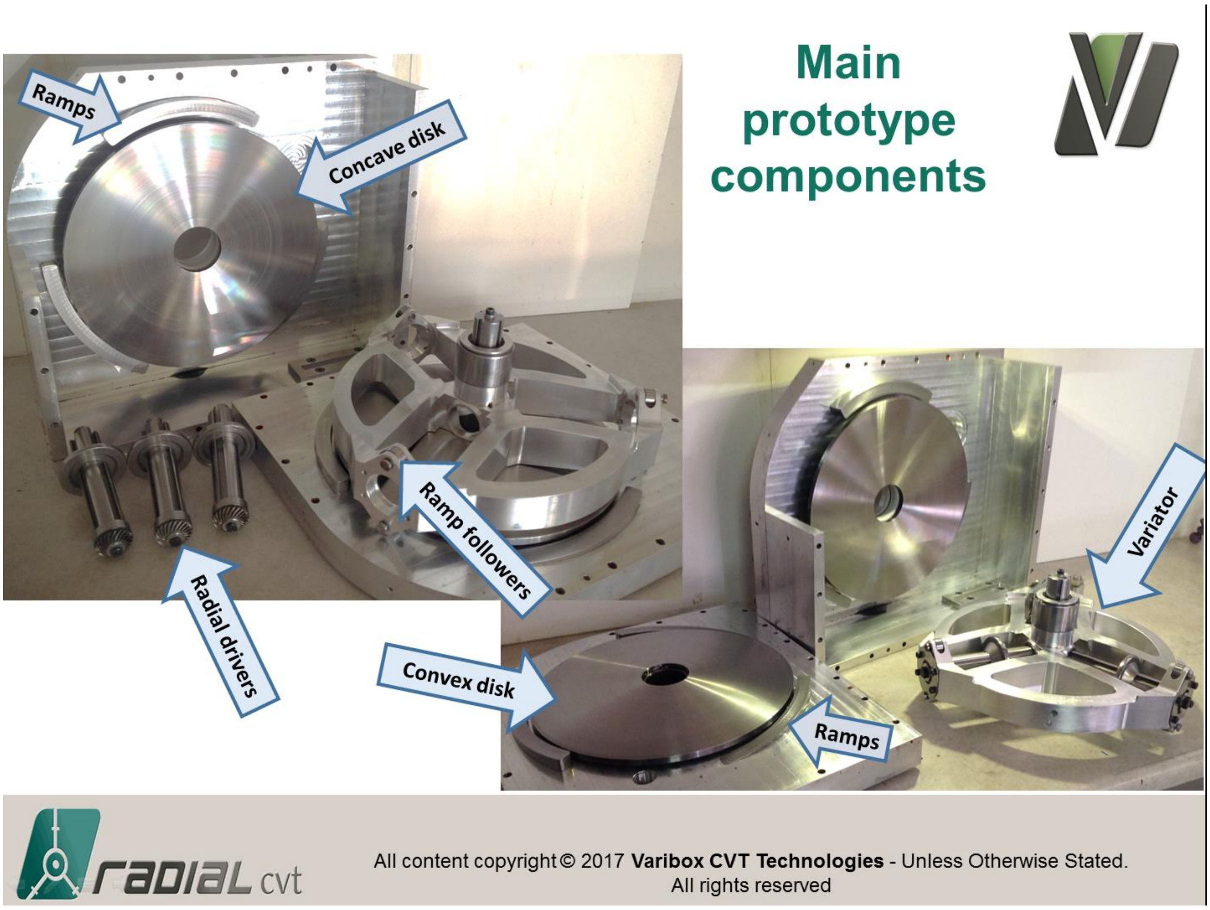

Dr. J. J. Naude **6 Oct 2017**

Version 1.12

Table of contents

List of Figures

1 Executive summary

This document provides a design and traction drive contact analysis and simulation of the first RADIALcvt prototype as well as some initial test result. The simulation results are discussed and improvements to the current design recommended. It presents a high mechanical efficiency and eliminates the use of a hydraulic control system. The RADIALcvt has a number of fundamental advantages that sets it apart from all other developmental and commercial CVT's and are listed below:

- **One friction interface:** Only one friction drive interface in series in a parallel power path. All other CVT's, developmental and commercial have 2 friction drive interfaces in series thus resulting in a compound friction loss. Thus if the friction contacts have the same efficiency then the RADIALcvt will have 50% of the friction drive losses of other CVT's. See section 4 and 5 for details.
- **Line contact:** The friction drive contact in the RADIALcvt friction drive can be a line contact, which is only possible in belt/chain CVT and cone ring CVT and not possible in toroidal and planet ball CVT's. Line contact reduces the maximum contact stress.
- **Constant input radius:** The RADIALcvt has a constant friction drive input radius. All other CVT have a variable input radius which results in high surface rolling speeds and lower coefficient of friction which require higher clamping forces. See section 4.
- **Six parallel power paths:** The RADIALcvt has at least 6 parallel power paths. Such a large number of parallel paths is only possible in planet ball CVT's.
- **Large output friction disk:** The output friction drive disk of the RADIALcvt can be positioned concentric and close to the engine flywheel and can approximate flywheel size. Thus the diameter of this output friction drive can be much larger than any of the belt/chain or toroidal or cone ring CVT output friction drive components. Due to this fact the RADIALcvt provides its highest efficiency in low ratios associated with city driving. See section 4 and 5 for details.
- **High power efficiency:** Above results in a RADIALcvt with a friction drive contact power efficiency in all ratios, under maximum engine torque, of about 95% in high ratio to about 98% in low ratio including in use, without a 2 speed AMT, with a ratio range up to 4.7, or with ratio range up to 10 and beyond with 2 speed AMT

integration. A ratio range of 10 is currently the maximum in the industry. See section 4 and 5 for details.

- **No hydraulic control:** As shown in section 4 and 5, the RADIALcvt can be realised without any hydraulic control. All current developmental and commercial CVT require a hydraulic control system.
- **Clamping force utilization:** In the RADIALcvt configuration, a unit of clamping force supports two parallel friction drive interfaces, while in all other developmental and commercial CVT’s only one friction drive interface is supported. Losses due to clamping forces should thus be 50% lower in the RADIALcvt. See section 5 for details.
- **Clamping force location:** The RADIALcvt clamping force, bearing losses are only associated with the RADIALcvt output, namely the Convex and Concave disks, while the RADIALcvt input, the radial drivers, are in equilibrium as mentioned in section 4.3.5. Thus these bearing losses, for a given clamping force, are only a function of the RADIALcvt output speed. This has the obvious low loss advantages in low output speed ratios. In contrast in all other CVT’s, the clamping force is associated with both the input and output speeds of the respective CVT, thus for a given clamping force the applicable speed for bearing loss calculation would be the average of the input and output speeds.
- **Low bearing losses:** Disk bearing (clamping) losses, which are a well-known source of traction drive losses (Loewenthal & Zaretsky, 1985), is a maximum of 2.5% in high ratio to about 1.5% in low ratio of transmitted power. See section 6 for details.

Since the RADIALcvt use existing very well developed traction/ friction drive technology, any potential licensee of our technology can very easily evaluate and verify the advantages of the RADIALcvt. The advantages of the RADIALcvt is realised by its unique patented configuration of components.

Prototype testing: The first loaded tests were performed on 3 October 2017 and the results are presented in section 8. The RADIALcvt loaded efficiency results of Figure 38 are in line with recently published results of a current in production CVT vs the Dana Variglide CVT (McIndoe G. V., 2016) (as presented in section 11, Figure 63). This is very encouraging for further RADIALcvt development, since the current RADIALcvt results are that of a first prototype while both the current production CVT and Dana Variglide have been in development for many years. As the simulation results of section 4 indicate as well as the fundamental advantages of the RADIALcvt, there is a lot of potential efficiency improvement still to be unlocked in the RADIALcvt configuration. These tests also prove that all the radial drivers run at the same diameter and that the ratio shifting mechanism operates successfully. Figure 39 is reproduced below in which the RADIALcvt efficiency is superimposed on the results from (McIndoe G. V., 2016).

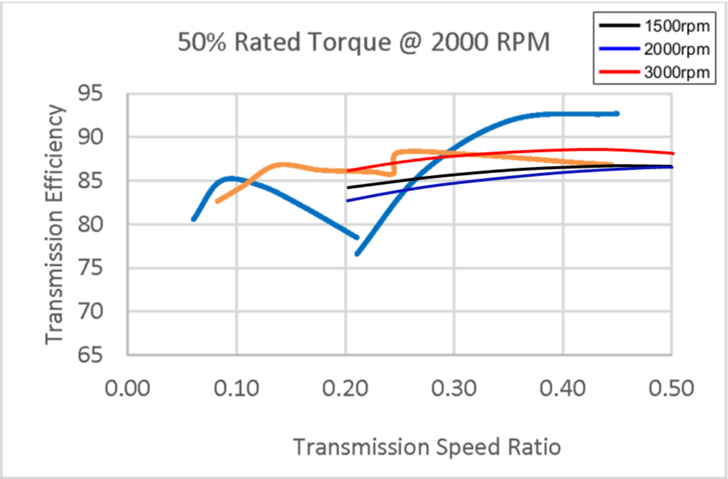

Figure 11. Comparison of Over All Transmission Efficiency.

Figure 1 Reproduced Figure 39

E^2 transmission configuration: Section 9 presents a concept design for a 225 N.m input E^2 transmission with a ratio range of 10, also featuring a hard geared low ratio and reverse as well as a loading cam system. The E^2 transmission does not need a variator ratio change when shifting form its First mode of operation to its Second.

Electric vehicle and Industrial geared motor configuration: Section 10 presents a RADIALcvt concept design for electric vehicles and industrial geared motor applications. This design eliminates the front disk drive passing on the outside of the disks, by introducing a configuration in which this drive passes through the centre of the disks.

Published efficiencies and comparisons: Section 11 include some published efficiencies of existing CVT's as well as some comparisons to other transmission performances in the automotive industry.

Published PCT: The RADIALcvt PCT patent application with search report was published and can be downloaded from:

https://worldwide.espacenet.com/publicationDetails/originalDocument?CC=WO&NR=2017143363A1&KC=A1&FT=D&ND=3&date=20170824&DB=EPODOC&locale=en_EP

The search report confirmed the novel configuration of the RADIALcvt and all 12 claims were granted without modification.

2 RADIALcvt specifications

The RADIALcvt presented in this document functions according to the PCT patent application number WO2017/143363 (Naude, 2017). The current prototype has the following specifications:

Input torque	70 N.m (extended to 225 N.m with AMT integration)
Maximum input rpm	4400
Disk diameter	292 mm
Width	262mm
Height	340 mm

Figure 1 presents a 3D CAD design of the RADIALcvt prototype. Note that in this design the combining planetary system is integrated in the rear of the rear convex disk, while in WO2017/143363 (Naude, 2017) it is positioned to one side.

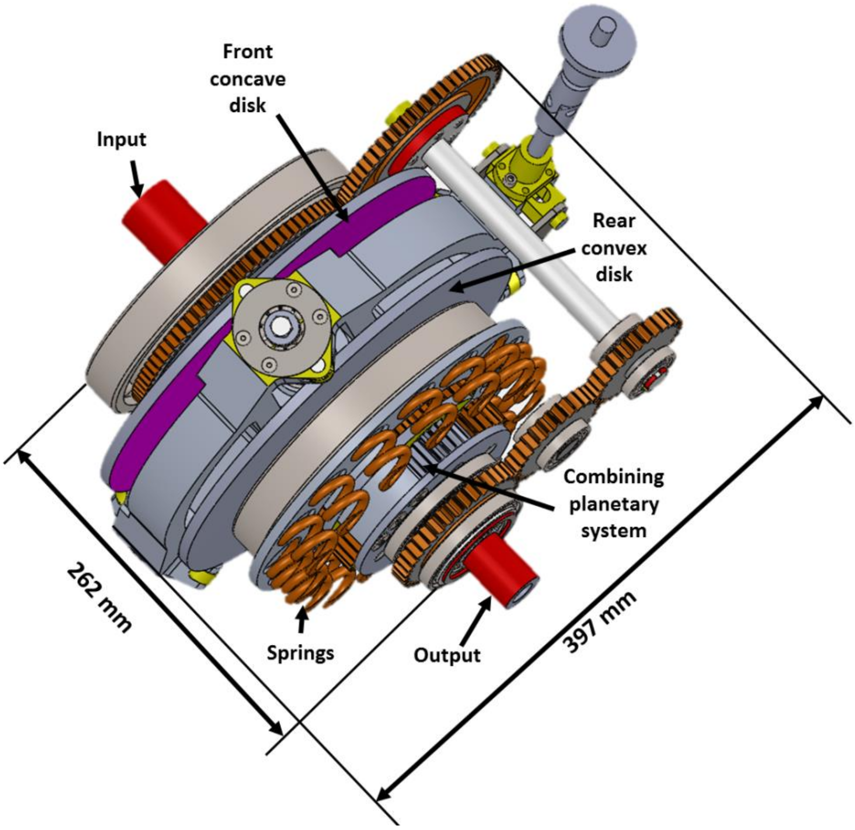

Figure 2. 3D CAD design of the RADIALcvt prototype

This design used the same variator configuration as in WO2017/143363 (Naude, 2017) that is with 3 radial drivers, making contact and driving the two disks in opposite directions in a traction fluid. Thus 6 traction drive contact points are created, representing the 6 parallel power paths, each parallel path containing only one friction drive interface in series. Two sets of ramps are employed, on either side of the variator configuration, engaging rollers on either side of the outer Radial shaft bearing, to position the variator in an axial position when ratio shifting is performed, whereas in WO2017/143363 (Naude, 2017) a single ramp with roller on both sides were employed.

3 Traction drive simulation

This section presents the simulation of the traction drive interface of a radial driver clamped between the convex and concave disk. This simulation is based on the design methodology as presented in (Loewenthal & Zaretsky, 1985). This work is based on regression analysis of a large number of experimental results using Santotrac 50 and TDF 88 as traction fluid. This methodology was also recently used, among others, by (Lichao, 2013) and (Carter, Pohl, Raney, & Sadler, 2004).

3.1 Geometry angles

Figure 2 presents the geometry of a driver clamped between disks in the y plane. The y direction is defined as the direction away from the coincident axes of rotation of body B (convex disk) and body C (concave disk). The notation used is the same as used in (Loewenthal & Zaretsky, 1985) page 26 and 27.

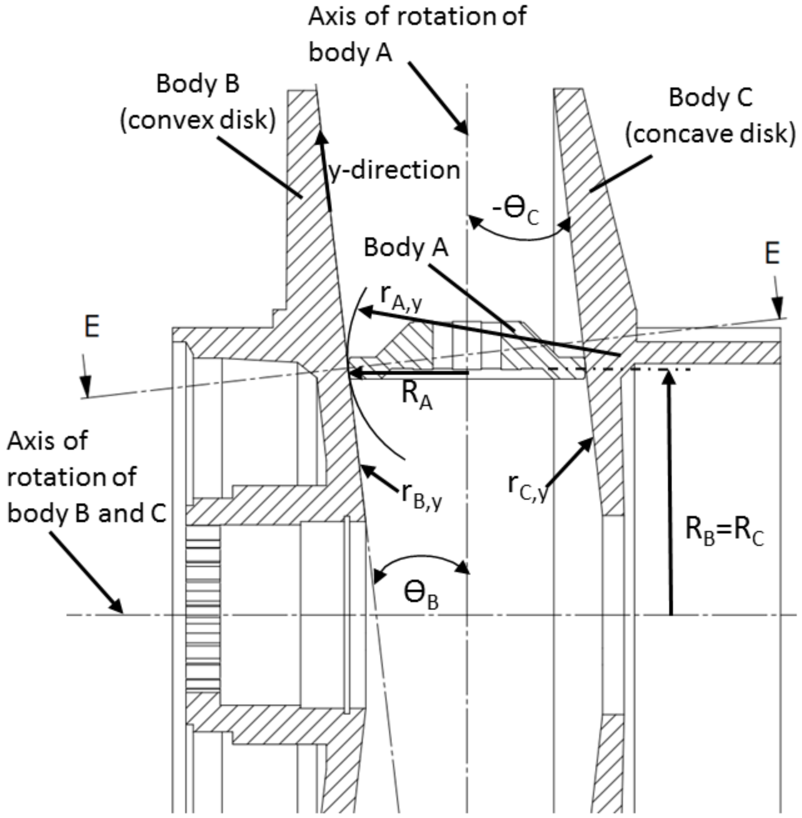

Figure 3 Geometry in the y-plane

Considering body A and B, the angle γ is defined as the angle between the axis of rotation of body A and B and is 90^0. Similarly γ for bodies A and C is also 90^0. Considering body A and B, the angle ϴ is defined as the angle between the rotation axis of body A and the line/plane tangent to the contact point. Θ_B refers to the interface between body A and B and Θ_C refers to the interface between body A and C. In the current RADIALcvt design the convex disk and concave disk have the same disk angle of 6.5^0.

Figure 4 below presents Figure 25 of (Loewenthal & Zaretsky, 1985) as it is used to determine ϴ for different traction drive configurations. From Figure 3 it is concluded that for the body A and B interface (most left configuration in the 3rd row) $\Theta_B=6.5^0$ and for body A and C interface (most left configuration in the 4th row) $\Theta_C=-6.5^0$. Note that in Figure 4 body A rotates around the horizontal axis

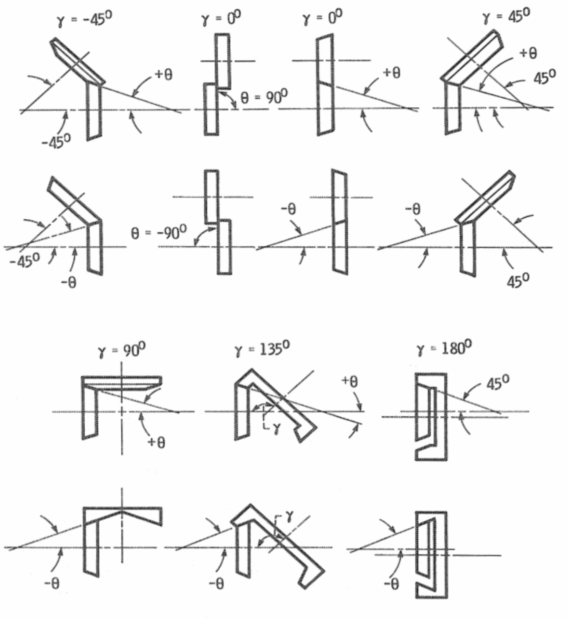

Figure 25.—Representative spin-producing geometries.

Figure 4 Body A and B configuration (Loewenthal & Zaretsky, 1985)

3.2 Geometry radiusses

Figure 5 presents a view of section E-E in Figure 3 which also presents the x direction/plane. The x-direction is defined as the rolling direction.

The following are the relevant radiuses and their values and value ranges of the current RADIALcvt prototype:

Body A

R_A=31 mm	Rolling radius of body A
$R_{A,x}$=31 mm	Contact radius of body A in the x direction
$R_{A,y}$=45 mm	Contact radius (crown) of body A in the y direction. This contact is also modelled as line contact in which case it has infinite value.
$R_{A,yline}$=2.35mm	In the case where $R_{A,y}$ is modelled as a line contact, this value refers to the length of the line contact.

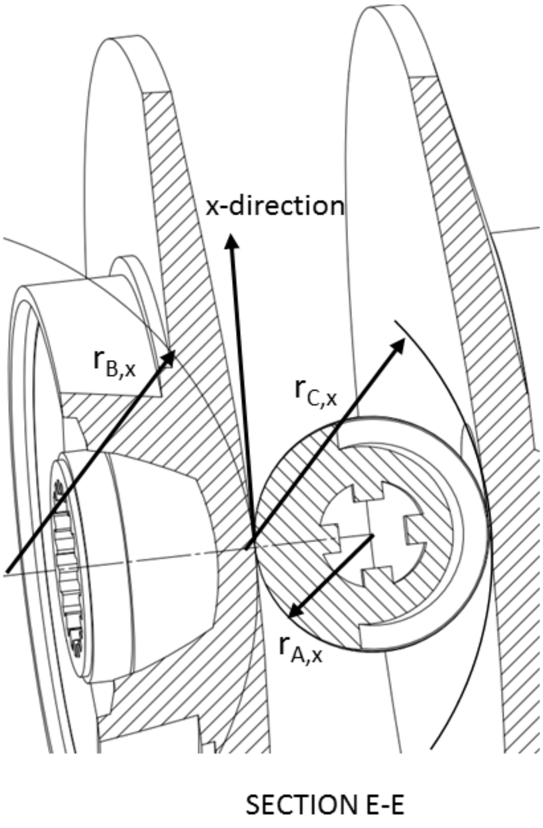

Figure 5 Geometry in the x-plane

Body B

R_B=30 - 143 mm	Variable rolling radius of body B
$R_{B,x}$	Contact radius of body B in the x-direction which is a function of R_B. $R_{B,x}$ is calculated by a Matlab function calculating the projected circle created by R_B projected on a plane tilted at an angle equal to the disk angle.

$R_{B,y}$=infinity	Contact radius of body B in the y direction. This contact is a line contact, thus the infinite value.
Body C	
R_C=30 - 143 mm	Variable rolling radius of body C
$R_{C,x}$	Contact radius of body C in the x direction which is a function of R_C. Note that $R_{C,x}$= -$R_{B,x}$ because of the negative radius. (Convex vs Concave)
$R_{C,y}$=infinity	Contact radius of body C in the y direction. This contact is a line contact, thus the infinite value.

During simulation R_B and R_C are varied, which caused $R_{C,x}$ and $R_{B,x}$ to vary while all the other above angles and radiuses are kept constant.

3.3 Operating parameters

The current RADIALcvt is intended as a hydraulic free CVT for small passenger vehicles, typically around 70 N.m, 40 kW torque and power. In these vehicles there is no need to operate the engine above 4400 rpm as at this point maximum power is achieved while maximum torque is achieved at lower rpm. Thus 4400 rpm is taken as the input speed and also the speed of the drivers (body A). The normal load, Q, in the traction contact is taken as 6800 N. The surface rolling speed in the x-direction, U, is calculated as U=4400 rpm*pi*2*R_A/60=14.3 m/s. Note that since the radius R_A=31 mm of body A does not change, U is also a constant, which is not the case in current commercial CVT or CVT's in development including, Cone ring, Toroidal and Planet ball CVT's. The fact that U is constant for the RADIALcvt is a huge advantage, because as U increases, the maximum traction coefficient decreases as reported by (Loewenthal & Rohn, 1983) figure 11, duplicated below as Figure 6.

The low maximum surface velocity, U=14.3 m/s, of the RADIALcvt prototype will thus contribute to a higher maximum traction coefficient. Figure 6 also indicates that maximum contact pressures above about 2 GPa do not increase the maximum traction coefficient. The lubricant inlet temperature is set at $\tilde{T}$ = 50 ^{0}C.

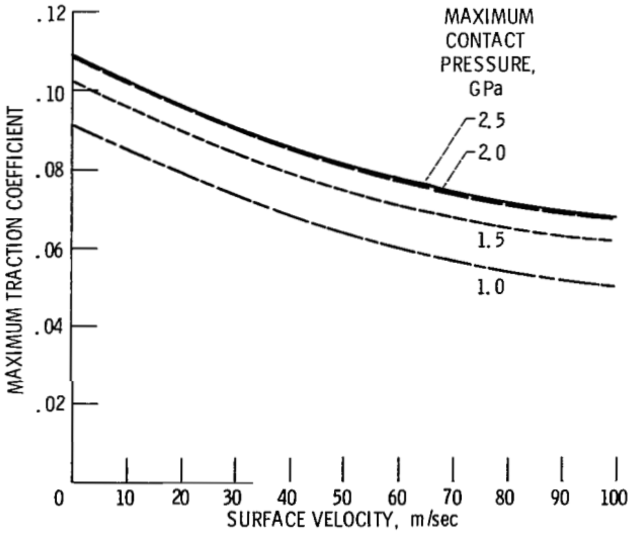

Figure 11. - Effect of surface velocity on maximum traction coefficient. Predicted from Santotrac 50 correlation. Temperature, 80° C; ellipticity ratio, 5; zero spin.

Figure 6 Surface velocity vs maximum traction coefficient (Loewenthal & Zaretsky, 1985)

3.4 Matlab simulation steps

The below section describes the sequence of calculations performed in the Matlab contact simulation.

1. **Calculate equivalent radii**

$$\frac{1}{R_x} = \frac{1}{r_{A,x}} + \frac{1}{r_{B,x}}$$

(Loewenthal & Zaretsky, 1985) equation 3

$$\frac{1}{R_y} = \frac{1}{r_{A,y}} + \frac{1}{r_{B,y}}$$

(Loewenthal & Zaretsky, 1985) equation 10

2. **Calculate contact parameters**

$$\rho = \frac{1}{R_x} + \frac{1}{R_y}$$

Inverse curvature sum (Loewenthal & Zaretsky, 1985) equation 17

$$g = \sqrt[3]{\frac{3Q}{2\rho}\left(\frac{1-\xi_A^2}{E_A} + \frac{1-\xi_B^2}{E_B}\right)}$$

Auxiliary contact size parameter (Loewenthal & Zaretsky, 1985) equation 16

Where $E_A = E_B = 207$ GPa representing the modulus of elasticity of steel and $\xi_A = \xi_B = 0.3$ representing the poison ratio for steel.

$$k = \left(\frac{R_y}{R_x}\right)^{2/\pi}$$

Elliptic ratio (Loewenthal & Zaretsky, 1985) equation 9

Figure 11 in (Loewenthal & Zaretsky, 1985) was digitised and used as a lookup for dimensionless contact ellipse factors a^* and b^* using k.

The contact elliptic radii are calculated as:

$$a = a^* g; \quad b = b^* g$$

Elliptic ratio (Loewenthal & Zaretsky, 1985) equation 14

3. Maximum contact stress

The maximum contact stress is calculated as:

$$\sigma_0 = \frac{3Q}{2\pi ab}$$

Maximum contact stress (Loewenthal & Zaretsky, 1985) equation 14

As a comparison, the maximum contact stress, σ_0, b and k are also calculated for Hertz cylinder-cylinder contact where $R_{A,yline}$=2a, while b and σ_0 is calculated via the Hertz formula and k from k=a/b.

4. Calculate spin, maximum traction coefficient and initial traction slope

Spin, ω_S, is the result of a mismatch in roller radii at contact points on either side of the point of pure rolling and is calculated by:

$$\frac{\omega_s}{U} = \frac{\sin\theta}{R_A} - \frac{\sin(\gamma - \theta)}{R_B}$$

(Loewenthal & Zaretsky, 1985) equation 36

Non dimensional spin is calculated as:

$$\omega_s \sqrt{ab} / U$$

(Loewenthal & Zaretsky, 1985) page 35

Use the regression results to calculate the maximum available traction coefficient, μ and the initial slope of the traction curve, m.

$$\mu = C_1 + C_2\sigma_0 + C_3\sigma_0^2 + C_4 U + C_5 U^2 + C_6 \widetilde{T} + C_7 k + C_8 \frac{\omega_s \sqrt{ab}}{U}$$

(Loewenthal & Zaretsky, 1985) equation 52

$$m = C_1 + C_2\sigma_0 + C_3 \ln \sigma_0 + C_4 U + C_5 U^2 + C_6 \widetilde{T} + C_7 k$$

Where the coefficients are presented in below table:

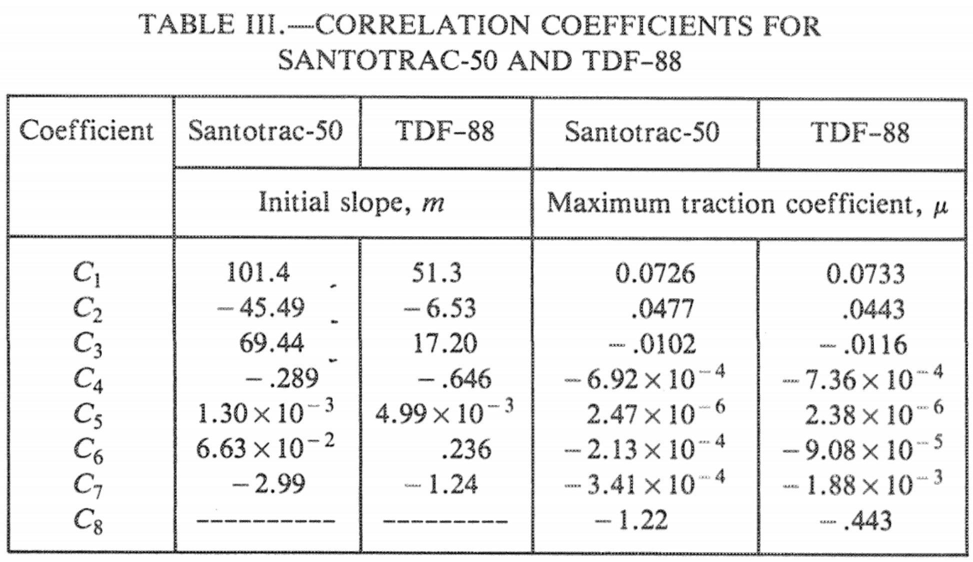

TABLE III.—CORRELATION COEFFICIENTS FOR SANTOTRAC-50 AND TDF-88

Coefficient	Santotrac-50	TDF-88	Santotrac-50	TDF-88
	Initial slope, m		Maximum traction coefficient, μ	
C_1	101.4	51.3	0.0726	0.0733
C_2	-45.49	-6.53	.0477	.0443
C_3	69.44	17.20	$-.0102$	$-.0116$
C_4	$-.289$	$-.646$	-6.92×10^{-4}	-7.36×10^{-4}
C_5	1.30×10^{-3}	4.99×10^{-3}	2.47×10^{-6}	2.38×10^{-6}
C_6	6.63×10^{-2}	.236	-2.13×10^{-4}	-9.08×10^{-5}
C_7	-2.99	-1.24	-3.41×10^{-4}	-1.88×10^{-3}
C_8	----------	---------	-1.22	$-.443$

Figure 7 Regression coefficients (Loewenthal & Zaretsky, 1985) page 35

Slope correction on m is performed by:

$$\frac{m^*}{m} = \left\{ \left(\frac{R_x}{R_x^*}\right)^{0.67} + 7.66\times10^{-3} m\sigma_0 e^{-0.21/k} \times \left[1 - A\left(\frac{R_x}{R_x^*}\right)^{0.67}\right]^{-1} \right\}$$

(Loewenthal & Zaretsky, 1985) equation 53

Where $A = 1.43 - 0.383/k + 0.0995/k^2$ and R_x^*=22.57mm for Santotrac 50 and 12.5mm for TDF-88.

The dimensionless spin parameter J_3, is calculated as:

$$J_3 = C\frac{\omega_s\sqrt{ab}}{U}$$

(Loewenthal & Zaretsky, 1985) equation 39

Where $C = \frac{3\pi}{8}\frac{m}{\mu}\sqrt{k}$ (Loewenthal & Zaretsky, 1985) equation 44

5. Slip/creep calculations

Slip or creep is the differential velocity, ΔU, in the rolling direction (x- direction) arising from the shear forces generated between body A and B across the lubricant film. If no slip exists, there is no traction and the coefficient of friction in the x-direction μ_X=0. It is therefore important to generate the relationship between ΔU and μ_X as ΔU increases while μ_X also increases to its maximum value. The graph detailing ΔU/U versus μ_X is used for this purpose and is referred to as the traction curve. In order to generate the traction curve, incremental values for ΔU/U from 0 to 0.07 (0% to 7%) is generated and the following is performed for each increment to calculate the respective μ_X value as well as traction in the y-direction, μ_Y value:

Dimensionless J_1 parameter is calculated as:

$$J_1 = C\frac{\Delta U}{U}$$

(Loewenthal & Zaretsky, 1985) equation 37

Figure 27 in (Loewenthal & Zaretsky, 1985) was digitised and used as a lookup for dimensionless traction in the x-direction parameter J_4 by using above J_1 and previously calculated J_3 and k values.

μ_X is now calculated from:

$$J_4 = \frac{\mu_x}{\mu}$$

(Loewenthal & Zaretsky, 1985) equation 40

Spin also generates a side traction force and this need to be calculated.

Figure 30 in (Loewenthal & Zaretsky, 1985) was digitised and used as a lookup for dimensionless side traction in the y-direction parameter J_5 by using above J_1 and previously calculated J_3 value.

μ_Y is now calculated from:

$$J_5 = \frac{\mu_y}{\mu}$$

(Loewenthal & Zaretsky, 1985) equation 41

By repeating above for each ΔU/U increment the traction curve can be plotted.

6. Selecting operating μ_X

Usually μ_X selected for operating conditions is a percentage of the maximum available μ_X value in the traction curve. For the purposes of this simulation the operating μ_X is set to 90% of the value of μ_X at 5% slip on the traction curve and the corresponding J_4 value is calculated as:

$$J_4 = \frac{\mu_X}{\mu}$$

(Loewenthal & Zaretsky, 1985) equation 40

Where μ_X now represents the value of μ_X under operating conditions at 5% slip level.

7. Power calculations

Transmitted power and torque

The transmitted power Pt is calculated as:

$P_t = \mu_X Q U$ (Loewenthal & Zaretsky, 1985) page 3

The transmitted input torque is calculated as:

$T_t = 60P_t/(2\pi \text{input rpm})$

Power traction contact loss

Figure 31 in (Loewenthal & Zaretsky, 1985) was digitised and used as a lookup for the power loss factor LF by using the above calculated values for J_4, J_3 and k.

The ratio of $\left(\frac{\text{Power loss}}{\text{Power input}}\right)$ for the contact loss can now be calculated from:

$$\text{LF} = \frac{J_7}{J_4} = C\left(\frac{\text{Power loss}}{\text{Power input}}\right)$$

(Loewenthal & Zaretsky, 1985) equation 45

The traction contact power loss is calculated as:

$P_C = \left(\frac{\text{Power loss}}{\text{Power input}}\right) P_t$

Rolling traction power loss

By estimating the central EHD film thickness, the power loss due to rolling of the traction contact can be determined.

The material elastic parameter is calculated as:

$$E' = \frac{2}{\left(\frac{1-\xi_A^2}{E_A} + \frac{1-\xi_B^2}{E_B}\right)}$$

(Loewenthal & Zaretsky, 1985) equation 6

The dimensionless EHD speed parameter is calculated as:

$$U_D = \frac{\eta_0 U}{E' R_x}$$

(Loewenthal & Zaretsky, 1985) equation 4

Where η_0 =0.0194 represents the absolute viscosity of the traction fluid (Santotrac 50) at ambient pressure.

The dimensionless EHD load parameter is calculated as:

$$W = \frac{Q}{E' R_x^2}$$

(Loewenthal & Zaretsky, 1985) equation 7

The dimensionless EHD materials parameter is calculated as:

$$G = \alpha_p E'$$

(Loewenthal & Zaretsky, 1985) equation 8

Where α_p =2.6x10^{-8} Pa^{-1} represents the pressure-viscosity coefficient of the traction fluid (Santotrac 50).

The dimensionless central EHD film thickness is calculated as:

$$H_c = 2.69\, U_D^{0.67} G^{0.53} W^{-0.067} (1 - 0.61 e^{-0.73k})$$

(Loewenthal & Zaretsky, 1985) equation 12

The central EHD film thickness h_c is calculated from:

$$H_c = \frac{h_c}{R_x}$$

(Loewenthal & Zaretsky, 1985) equation 2

The rolling traction power loss is calculated as:

$$P_r = 9 \times 10^7\, h_c l U$$

(Loewenthal & Zaretsky, 1985) equation 2

Where the length of line contact $l = 2a$

Hysteresis power loss

The hysteresis power loss is calculated as:

$$P_h = F_h U = \frac{3}{16} \varphi \frac{b}{R_x} Q U$$

(Loewenthal & Zaretsky, 1985) equation 51 and page 38

Where the hysteresis loss factor for steel is φ=0.01

Total power loss and power efficiency

The total power loss is calculated as:

$P_{loss}= P_C+ P_r+ P_h$

The percentage power efficiency is calculated as:

$P_{eff}=100(P_t - P_{loss})/P_t$

8. Surface finish calculations

The ratio of film thickness to composite roughness, λ is set to 2 to avoid surface distress. The composite roughness σ is then calculated from:

$\lambda = h_C/\sigma$ (Loewenthal & Zaretsky, 1985) page 38

Therefore the actual composite surface roughness should be less than above calculated σ.

Assuming equal surface roughness, R_{Aq}, of body A and R_{Bq}, of body B, the maximum surface roughness, R_q, of body A and B is calculated from:

$R_q=(\sigma^2/2)^{0.5}$ (Leimei, 2013) equation 2

Where $\sigma = (R_{Aq}{}^2 + R_{Bq}{}^2)^{0.5}$

Matlab code was generated to calculate above. The Matlab results were compared against the Performance calculation example in section 3.3 of (Loewenthal & Zaretsky, 1985) page 35 to 38 to ensure correctness.

The use of the regression analysis is valid for the parameter ranges in Figure 8 below.

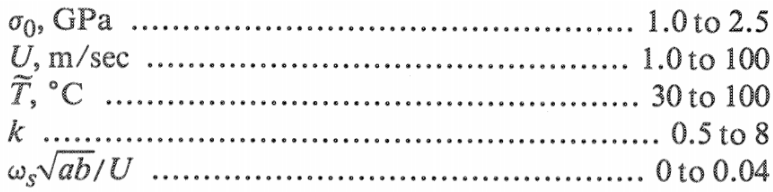

σ_0, GPa	1.0 to 2.5
U, m/sec	1.0 to 100
$\widetilde{T}$, °C	30 to 100
k	0.5 to 8
$\omega_S\sqrt{ab}/U$	0 to 0.04

Figure 8 Regression analysis parameter ranges (Loewenthal & Zaretsky, 1985)

4 Matlab simulation results

Matlab results are presented in the form of graphs, each including the relevant results for both body A and body B(Convex disk) and for body A and body C(Concave disk).

Since all current commercial CVT and developmental CVT include a variable input radius, a complex hydraulic control/clamping system is used to vary Q when the input radius varies. This is required since the tangential contact traction force changes (assuming input torque is unchanged) as the radius changes. What complicates the matter even further is that two contact friction drives, including at least two variable radii needs to be optimised by a single clamping mechanism in toroidal CVT's. In belt CVT's two clamping actuators is used, one at each pulley, but need to be synchronised to maintain the current ratio as torque demand changes. Controlling slip seems to be a dominant control strategy in current commercial and developmental CVT's. Referring for example to (Jans, 2005), the Cone Ring CVT performs at maximum traction coefficient at 2% slip and the control system was developed to maintain this level of slip. Control can be simplified to account for torque changes by using a loading cam. The variable surface rolling speed in commercial and developmental CVT's adds yet another layer of complexity to the control system, since all of them create a very significant overdrive in high ratio, resulting in component speeds of more than double engine/input speed, with the resulting increase in rolling surface speed and the subsequent drop in traction coefficient thus requiring a higher clamping force, Q, to maintain current torque transfer levels. This also leads to more contact cycles and reduces life of the components. As an example typical operating traction coefficients reported by Torotrak (Heumann, Briffet, & Burke, 2003) varied from 0.035 to 0.055. All current commercial and developmental CVT's have two friction interfaces in series, resulting in compounded losses.

The RADIALcvt has two very significant fundamental advantages in comparison to above.

- **Only one friction contact**: The RADIALcvt has only one friction drive contact in series in its parallel power paths and there are therefore no compound losses.
- **Constant rolling speed**: The maximum surface rolling speed U, is constant through the ratio range for a given input rpm and is very low at a maximum of 14.3 m/s. Thus for engine input from idle to 4400 rpm, U changes from 3.25 m/s to 14.3 m/s. Figure

6 indicates that above rolling speed range is on the left hand side and will therefore not contribute in the reduction of the maximum traction coefficient as is the case in commercial and developmental CVT’s

4.1 Traction curves, spin and max traction coefficient

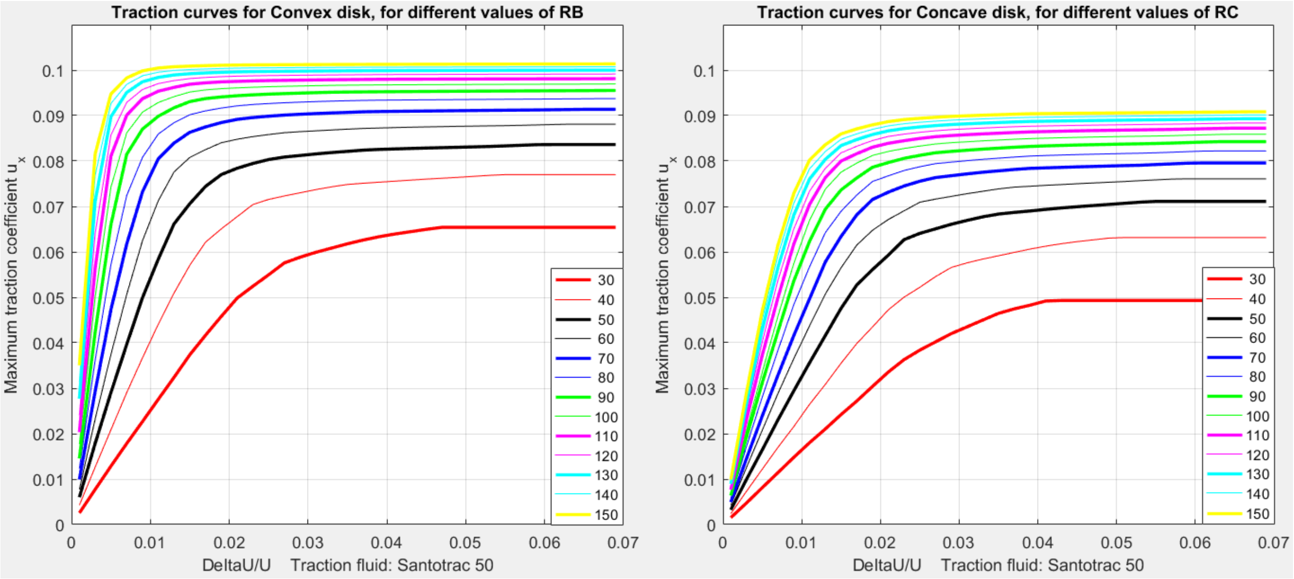

Figure 9 Traction curves

Figure 9 presents the traction curves for the Convex (R_B) disk and Concave(R_C) disk for different values of R_B and R_C. It can be seen that on average the maximum traction coefficient is 0.01 lower in the Concave disk in comparison to the Convex disk. Also small disk radii result in low maximum traction coefficients which exponentially increase with an increase in disk radius. Typically increasing the minimum disk radius from 30mm to 40mm will result in an about 0.013 increase in the maximum traction coefficient.

Evaluating Figure 10 and Figure 11 the following can be concluded:

- From the power loss contribution presented in Figure 10 is can be seen that the Traction contact power loss P_C is the only major contributor to power loss. P_C is a function of the loss factor LF which is a function of J_4, J_3 and k. Of these parameters, J_3 dominates and is directly related to spin via (Loewenthal & Zaretsky, 1985) equation 39 and also as reported by (Lichao, 2013).

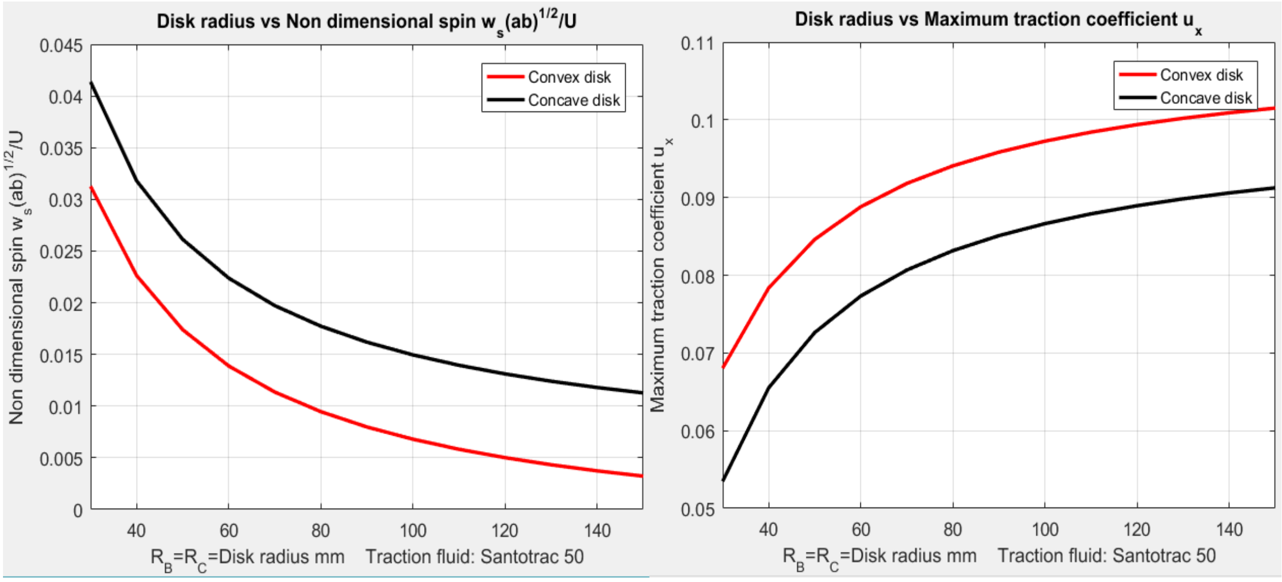

Figure 10 Spin and maximum traction coefficient

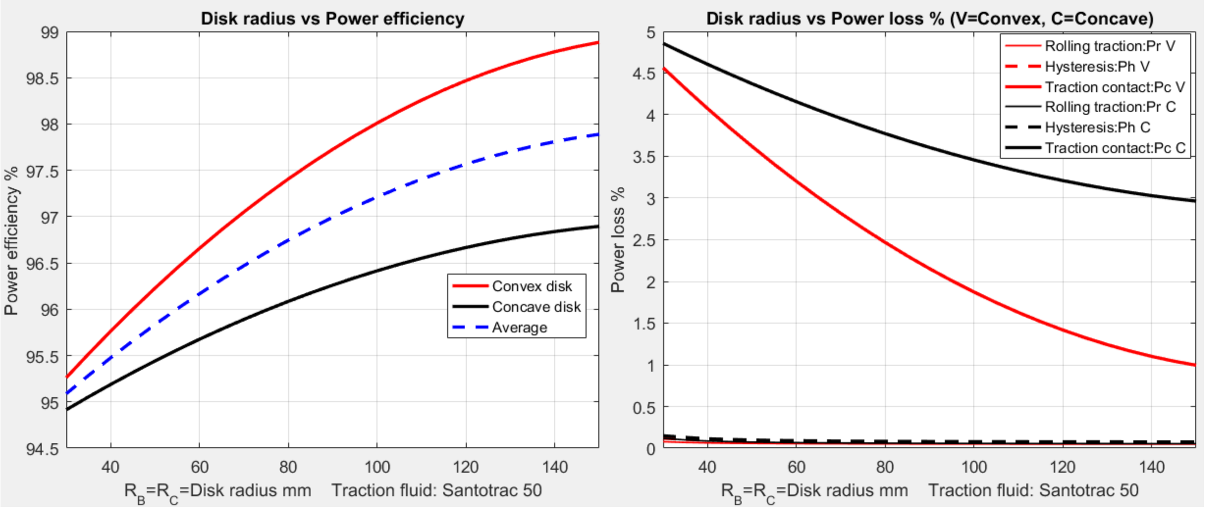

Figure 11 Power efficiency and power losses

- The source of spin, ω_S, is the result of a mismatch in body A and body B radii at contact points on either side of the point of pure rolling and is calculated by $\frac{\omega_s}{U} = \frac{\sin\theta}{R_A} - \frac{\sin(\gamma-\theta)}{R_B}$ as presented in section 3.4. Spin is zero when the line tangent to the contact point intersects the intersection of the rotating axes of body A and body B. Therefore if spin needs to be reduced at the low disk radii then for the convex disk, Θ_B need to be increased at these radii or R_A needs to be decreased and/or R_B increased. (Assuming close to equal R_B and R_A then $\Theta_B = 45^0$ will result in zero spin)

Similarly, for the concave disk, spin can be reduced by decreasing R_A and/or increasing R_B or in this case, Θ_C being negative, needs to be less negative or positive.

- However the radial adjustment of body A (to adjust the ratio) is dependent on a disk angle. If the disk angle is zero ($\Theta_B = \Theta_C = 0$) then the axis of body A needs to be at an angle other than 90^0 to the axes of body B and C in order to shift ratios. This will represent the only configuration in which the performance of the two disks is identical. Performance optimisation will therefore include the comparison of the combined performance of the convex and concave disk when Θ_B and Θ_C are not equal, to the configuration where body B and body C are flat disks while body A axis is at an angle other than 90^0 to the axis of body B and C. The current first prototype will provide a lot of insights into its shifting characteristics.

- To counter the effect of the lower maximum traction coefficient at low R_B and R_C the profile of the convex disk and concave disk can be modified to have a variable angle Θ_B and or Θ_C angle in such a way as to decrease the distance between these disks at low values of R_B and R_C. The effect will be that the two disks will be forced further apart when body A makes contact in this region. Since the clamping force is supplied by mechanical springs, the springs will be further compressed and the clamping force will increase accordingly to maintain the current torque level by compensating for the lower maximum traction coefficient. For example the current prototype springs are compressed 4mm, thus if above method is applied and for example if the springs are just compressed an additional 1mm this will result in a 25% increase in the clamping force.

- It is also very important to note that the high R_B and R_C values correspond to the low RADIALcvt ratios at pull away. Thus in city driving the RADIALcvt will operate in its very high power efficiency range typically under lower power loads. Current commercial CVT have difficulty in obtaining high power efficiency in these conditions, particularly because of the hydraulic control system.

- Thus for a very basic RADIALcvt, assuming low maximum contact stresses, typically below 2 GPa, the clamping force can be constant and thus created by mechanical springs. This however will result in over clamping at partial load, but the associated efficiency loss needs to be compared to the cost of a loading cam.

- When a more powerful RADIALcvt is considered, the same basic design is used, and maximum clamping force can be increased to say 2.5 GPa while employing a loading cam in combination with mechanical springs to optimize clamping vs input torque. This loading cam can be based on input torque as presented in section 4.3.5.

4.2 Elliptic ratio, maximum contact stress and power efficiency

The elliptic ratio k, a and b plays an important role in both the maximum contact stress and spin. Ideally a high value of b (semi width of contact area in the x or rolling direction) is desired with lower values of a (semi width of contact area in the y- direction transverse to the rolling direction) to produce lower values of k=a/b. However the larger the area created by the ellipse with radii a and b the lower the maximum contact stress. Line contact between body A and B as well as A and C is very effective in reducing the maximum contact stress. However line contact is only possible throughout the ratio range for constant values of Θ_B and Θ_C while this line contact l=2a is in the y direction, so care should be taken that it does not have a significant effect on increasing spin losses.

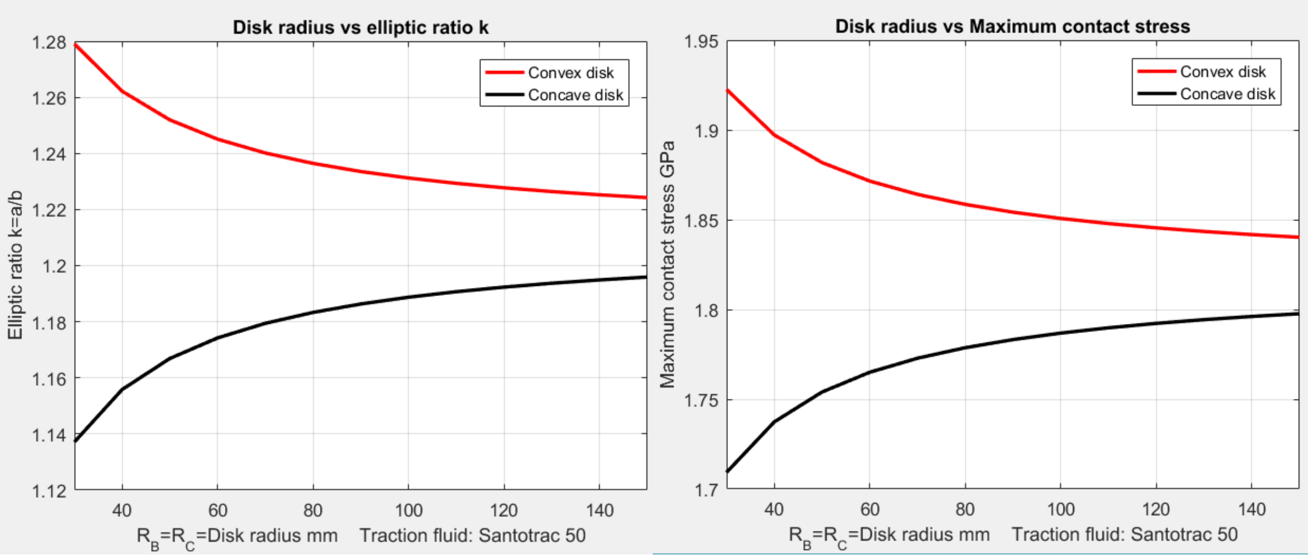

Figure 12 Maximum contact stress and elliptic ratio

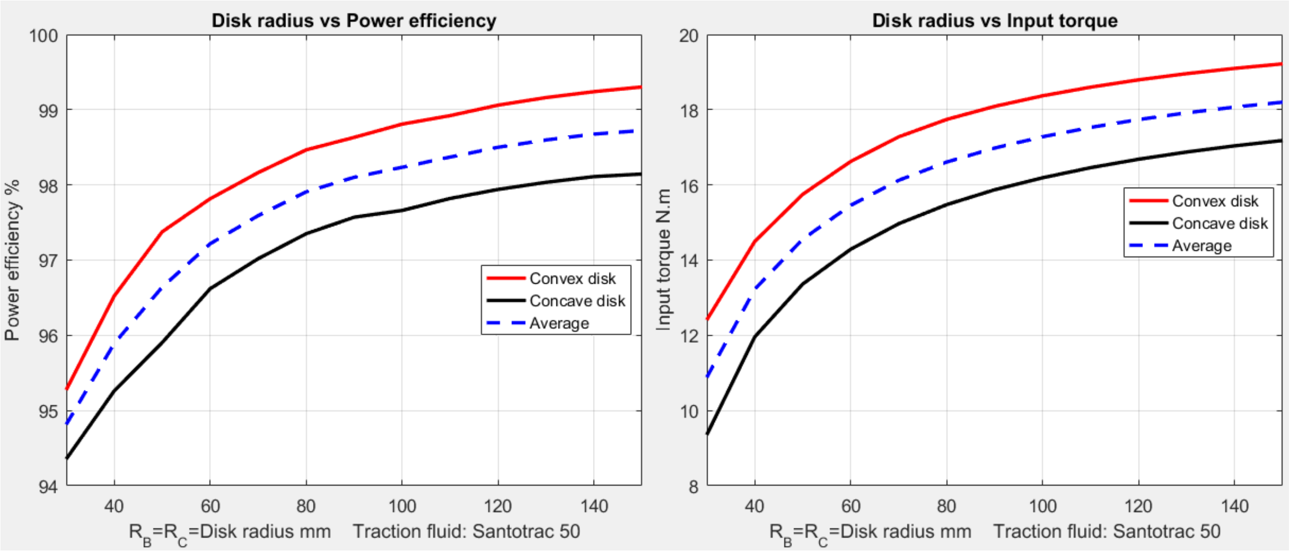

Figure 13 Power efficiency and Input torque

Evaluating Figure 12 and Figure 13 the following conclusions can be made:

- The convex disk produces higher k and maximum contact stresses while all stresses is below 2 GPa in the current design.
- Power efficiency is generally very high, average from about 95% to 98.5%, with the convex disk typically 1% higher than the concave disk.
- Average torque increase from low values of R_B and R_C from about 11 N.m to 18N.m while the Convex disk torque is generally about 2 N.m higher.
- Note the total torque of the current RADIALcvt is obtained by multiplying above average torque by the 6 parallel power paths, thus from about 66 N.m to 108 N.m. and 30 kW to 50 kW Figure 14 presents the input power and torque of the complete RADIALcvt.

Figure 15 presents the central film thickness h_c and the minimum surface roughness R_q for above conditions. It can be seen that a surface roughness of about 0.4 um on both the radial driver and disks will prevent metal on metal contact.

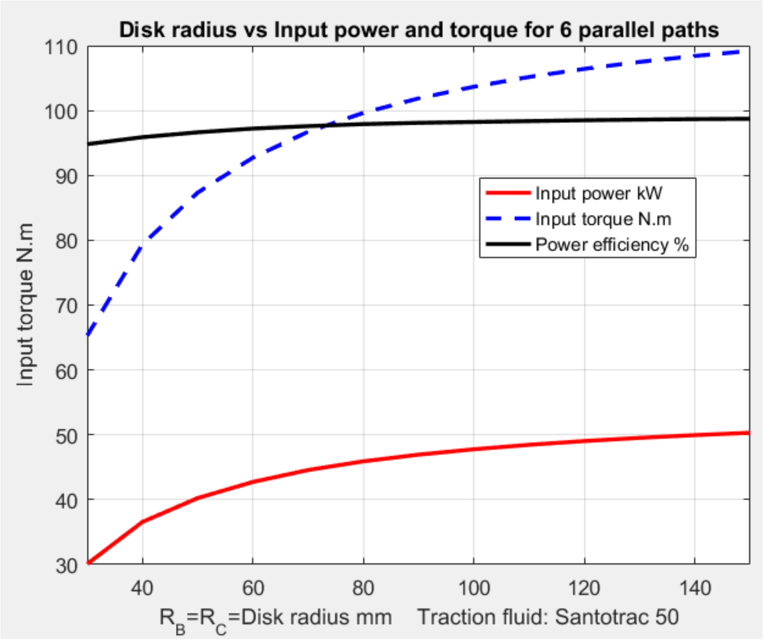

Figure 14 Input power, torque and power efficiency for the complete RADIALcvt

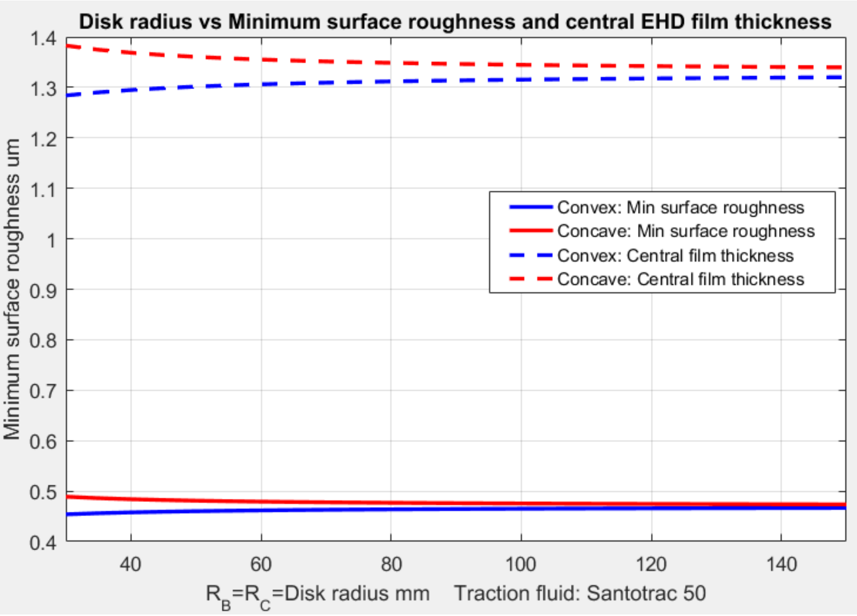

Figure 15 Minimum surface roughness and EHD film thickness

4.3 Comments on optimization

4.3.1 Increasing maximum disk size

The current RADIALcvt has a disk diameter of 292mm. In the case of a front wheel drive transmission the standard is that the differential axis is 180mm from the engine/RADIALcvt input axis. If it is assumed that a 25mm driveshaft has to pass over the disks, the disk diameter can be increased to 335 and typically the R_B and R_C range can be increased from

143mm to 165mm. If a ratio range of 4.5, equal to the current equivalent manual transmission is chosen, the minimum value of R_B and R_C will increase from 30mm to 37mm. Above results in a 0.5% increase at the minimum value of R_B and R_C in power efficiency from 95% to 95.5%.

4.3.2 Varying planetary system e value

From Figure 13 it can be seen that the input torque of the Concave disk is consistently lower than that of the Convex disk. If left unattended, the Concave disk torque will always represent the maximum input torque for both the Concave and Convex disk for an equally balanced planetary system with e value of -1 if calculated according to (Shingley & Miscke, 1989) page 553, which results in an equal 50% torque contribution of both the Convex and Concave disk to the Combining planetary system of Figure 2. By changing the e value of the Combining planetary system the torque contribution between the Convex and the Concave disk can be changed to such a ratio as to compensate for the difference in maximum toque capability of the two disks. Such a non-equal ratio will allow each disk to produce its respective maximum torque for the same clamping force. (Shingley & Miscke, 1989)

4.3.3 Integrating a two speed AMT

If a more power full RADIALcvt is considered and if it needs to compete with the current maximum ratio range on the market, around 10, then the following can be done:

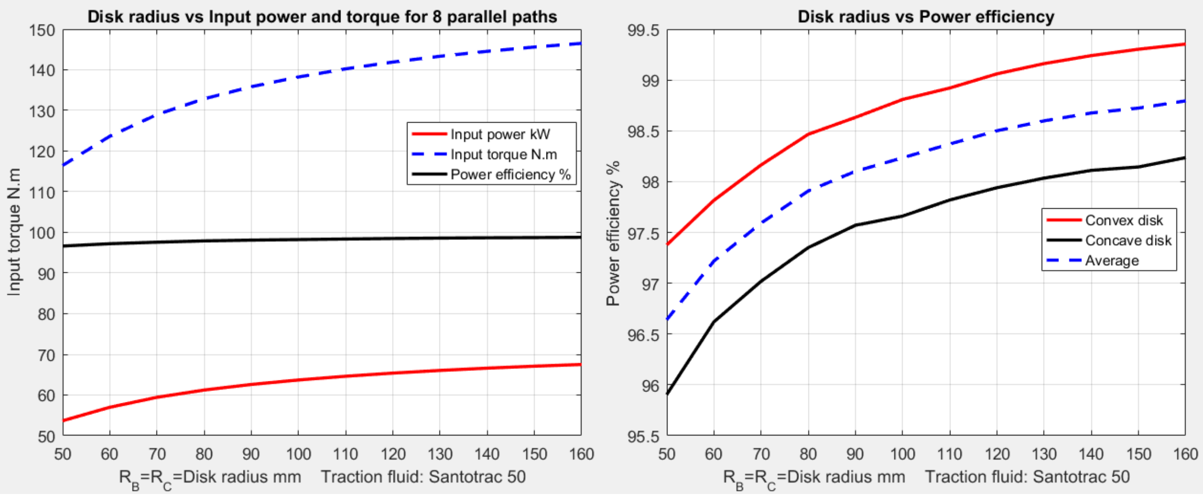

Figure 16 Effect of 2 speed AMT integration

- A two speed automated manual transmission can be integrated and this will require the RADIALcvt variator to only produce a ratio range of $10^{1/2}=3.16$.

- Taking above maximum R_B and R_C value of 165 and ignoring the fact that a more powerful engine will have a bigger flywheel and therefore allow bigger disks, the operating range of R_B and R_C is decreased to 165/3.16=52.2 to 165 mm.
- Above will create space around the input bevel gear and will allow the addition of another radial drive (body A) resulting in 8 parallel power paths vs the current 6.

Figure 16 presents the results of above with minimum power efficiency of about 96.6% in high ratio to about 98.7% in low ratio.

4.3.4 Increase line contact length

Increasing the line contact from 2.35 mm to 5 mm reduces the maximum contact stress, but increase a and therefore also k which leads to an increase in spin and lowering the power efficiency. Increasing the normal load Q to 15600 N, still produces contact stresses below 2 GPa but increases minimum input torque and power to 225 N.m and 100 kW respectively as presented in Figure 17. Above is accomplished with the sacrifice of about 1.25 % in minimum power efficiency of which the average is still above 95 %. The huge advantage is the input torque and power is about double the levels before the line contact increase as presented in Figure 16.

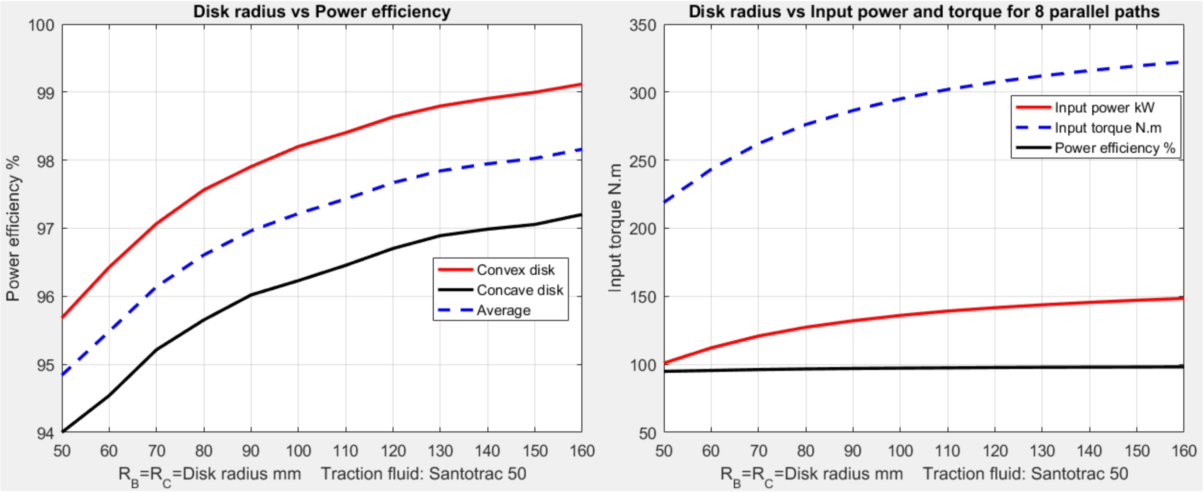

Figure 17 Effect of 2 speed AMT integration and line contact length increase

From Figure 18 it can be seen that spin level decrease as a result of the AMT integration (increase in the minimum R_B and R_C values), but again increased with the line contact length increase to more or less the same levels as that of Figure 10.

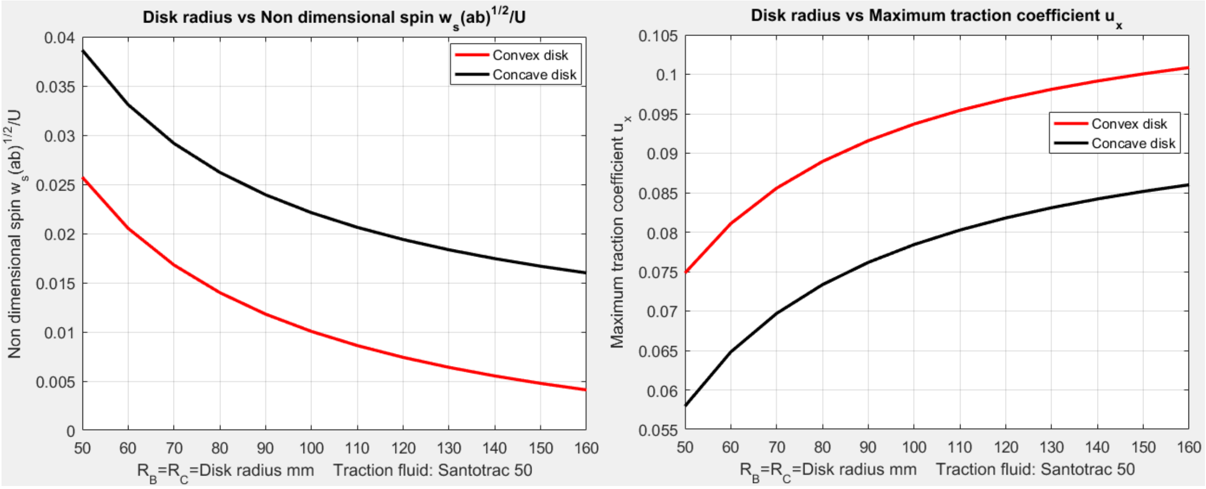

Figure 18 Line contact increase effect on spin and maximum traction coefficient.

4.3.5 Different Θ angles and a loading cam

Note that line contact are maintained, if different fixed angles of Θ_B and Θ_C are used, while this difference will create a variable normal load Q, created by mechanical springs, which can be used to compensate for the lower maximum traction coefficient at low R_B and R_C values. This will then also prevent over clamping in high values of R_B and R_C. Note that all of above is based on maximum contact stress values of less than 2 GPa, which is very low compared to industry standards.

In case where over clamping due to partial loads occur, the cost penalty to implement a loading cam need to be considered and compared to the power efficiency gain.

The configuration of the RADIALcvt variator facilitates the implementation of a loading cam in the following way. The structure, in which the radial drivers are housed, has a reaction torque around its axis (coinciding with the axis of the input shaft) which is equal to the input torque. The reason for this being the fact that each radial driver (body A) is subject to a tangential traction force in each of the two contacts with the convex a concave disk. These forces are substantially equal but in opposite directions, thus cancelling each other.

Thus for the implementation of a loading cam the above structure, housing the radial drivers, can be coupled (which may include a torque multiplying gear ratio) to a loading cam operation between one of the disk bearings and the RADIALcvt casing.

With above in place the combination of different fixed angles of Θ_B and Θ_C together with mechanical springs and the addition of a loading cam as per above would prevent over clamping in all operating conditions of the RADIALcvt.

5 Contact simulation summary

In general considering the high levels of power efficiency which should result in low operating temperatures and relative high maximum traction coefficients at relative low maximum contact stresses (below 2 GPa) the following:

- Other traction fluids should be investigate that under low temperatures and low contact stresses provide better maximum traction coefficients at higher levels of spin. (Loewenthal & Zaretsky, 1985) indicates that softer traction fluids (lower slope m) with thicker film thickness are more tolerant of spin.
- Note that all of above is under the assumption that engine torque and power does not need to be limited in some ratios as is the case with commercial CVT's. Therefore the RADIALcvt relies on the fact that it can, in all ratios, handle any maximum torque the engine can create, thus eliminating any engine power or torque limiting control system.

5.1 Without AMT integration

Without AMT integration, the spin levels are already high and therefore any contact line increase will further lower the maximum traction fluid and power efficiency. The performance of the contact line in question does not vary too much from a crowned surface in terms of contact stresses, thus in this case variable Θ_B and Θ_C angles can be used to counter spin and vary clamping force to compensate for lower maximum traction coefficient. Ratio range for the current prototype is 4.7 and seems to be close to a maximum because of the available space. Minimum power and torque levels are at 30 kW and 66 N.m respectively.

5.2 With 2 speed AMT integration

With AMT integration the ratio range is reduced to 3.16 to provide a CVT with an overall ratio range of 10, equalling the maximum currently in the industry. The reduced ratio range, enables larger minimum R_B and R_C values which in turn reduce spin, increase traction coefficient and power efficiency while also allow space for the inclusion of a fourth radial drive (body A) thus creating 8 parallel power paths.

If Θ_B and Θ_C are kept fixed, line contact is possible in all ratios and by increasing the line contact reduces the maximum contact stress. The downside of line contact is an increase in spin, resulting in lower maximum traction coefficient and lower power efficiency.

However by increasing the contact line length from 2.3mm to 5mm and increasing the normal load Q to 15600 N, while still keeping maximum contact stresses below 2 GPa, produces a 225 N.m, 100 kW CVT with a minimum power efficiency of 95 %. The penalty for the line contact increase is about 1.25 % in power efficiency. Note that line contact is not possible in toroidal or planet ball CVT's. This is thus a major advantage of the RADIALcvt.

Yet another advantage of the RADIALcvt in comparison to chain/belt CVT's is the fact that the disks in the RADIALcvt are uniformly loaded. In chain/belt CVT's the chain/belt only makes contact on the one side of the disks creating a force that tends to push the disks away from each other on only one side. To counter this involves stiffer disks, shafts and bearings to deal with this.

Yet another advantage of the RADIALcvt compared to current commercial and developmental CVT's is the fact that in the case of the RADIALcvt, one unit of clamping force supports 2 parallel power paths. In the case of toroidal and planet ball CVT's a unit of clamping force support two friction drive contacts point (input toroid to roller to output toroid) of a single friction drive path with two friction drive contacts in series. In belt/chain CVT's for the input pulley a unit of clamping force supports two friction contact interfaces on either side of the belt/chain which represents two parallel power paths, but since an output pulley is also required the total belt/chain CVT with two pulleys and their respective clamping forces also result in two friction drive interfaces for each unit of clamping force, the same as for the toroidal CVT's. However note that in belt/chain CVT's the clamping force is not applied across bearings, thus they do not suffer the effect of bearing loss due to clamping force. However the camping force creates a belt/chain tension force which tends to pull the two pulleys towards each other and therefore the bearings being loaded with this force suffer the relevant losses indirectly caused by the clamping force.

In high efficiency traction drives, the losses in the bearings supporting the clamping force can be a major contributor to the overall losses in the CVT (Loewenthal & Zaretsky, 1985). Above provides the RADIALcvt with a fundamental advantage with the potential of having only 50% of the clamping bearing losses if compared to belt/chain, toroidal, planet ball and cone ring CVT’s.

6 Bearing loss analysis

6.1 Disk bearings

The disk bearings presented in Figure 2 is for use in a RADIALcvt display version with perspex casing plates and is not suited for efficiency testing because of their large diameter which will result in large bearing losses as well as the fact that deep groove bearings create relatively large losses when loaded axially. Disk bearings for use in the RADIALcvt have to serve the following purposes:

1. Bear the clamping force create by the mechanical springs.
2. Stabilize the variator structure relative to the disks and RADIALcvt casing.
3. Have minimal power losses.

The variator structure is centralised around the output axis via a bush in the front casing and at the rear via a bearing located in the convex disk. However if not at least one disk is secured parallel to the variator structure, the two disk might not be parallel and this will cause a difference in the radius of the three drivers with respect to the input shaft axis. This is of particular concern when the RADIALcvt is in the high ratio (radial driver are at a minimum radius with respect to the input shaft axis). Thus to secure and stabilize the convex disk, its bearing location need to be at a relative large radius, as in the current prototype design, but without the typical losses associated with large diameter bearings.

Figure 19 presents a design which supports the convex disk at a relative large radius by using three Bearing units mounted with their axis in the radial direction from the input shaft in a Clamping unit. The Clamping unit is mounted in the casing of the RADIALcvt via the mating of its outer Circular body with a circular cut out in the casing and is axially slidable relative to the casing. An angled surface (green) on the Bearing units make line contact with a mating Disk angled surface (green) on the rear of the Convex disk. This angled surface is at such an angle that the line contact does not experience any spin and therefore consists of pure rolling. A Center bearing in the Clamping structure, mating with a Center boss on the Convex disk rear secures the Convex disk concentric to the Clamping structure. The Clamping springs acts between the Clamping unit and the RADIALcvt casing to force the Convex disk via the mating green surface against the radial drivers.

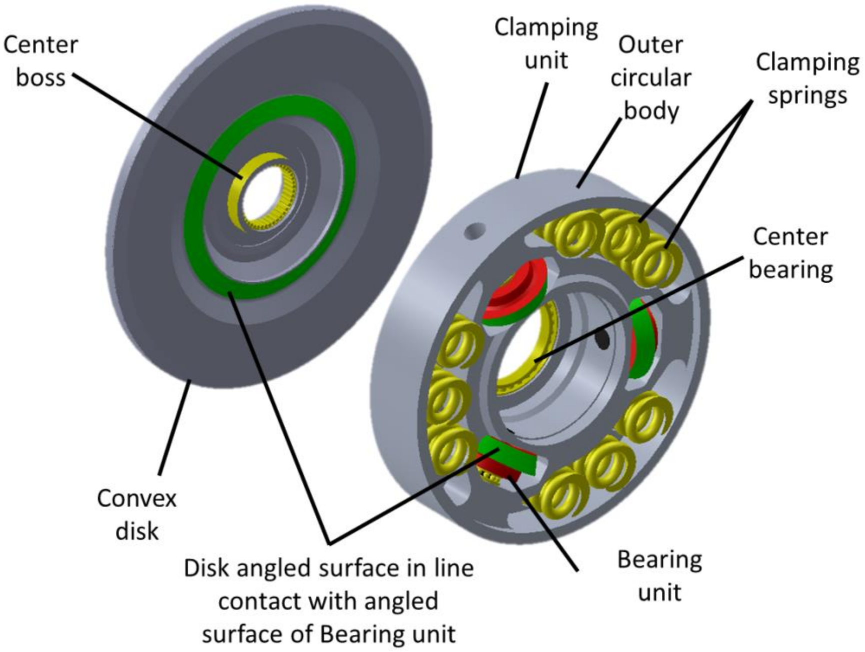

Figure 19 Clamping unit and Convex disk

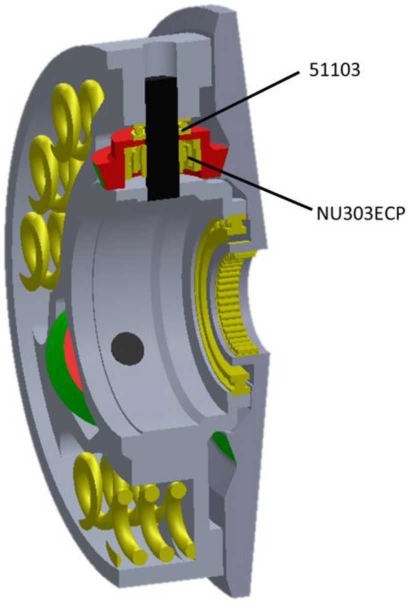

Figure 20 Cross section of assembled Convex disk and Clamping unit

Figure 19 presents a cross section of the assembled Clamping unit and Convex disk. The Bearing units consist of a NU303ECP cylindrical roller bearing to handle the radial load, while a 51103 thrust ball bearing handles the axial load created by the angled green line contact surface. The size of the Bearing unit and its line contact radius with the Convex disk is such that the Bearing unit turns 2.17 times faster than the Convex disk. It is assumed that the

NU303ECP bearings bear the full clamping force in their radial direction and that the 51103 bear 0.35 (angled surface at 19.4^0) of the clamping force in their axial direction.

The Concave disk is simply supported via a 51113 thrust ball bearing. Figure 21 to Figure 23 presents sample calculations of above bearings from the online SKF bearing calculator (SKF, SKF) for a disk speed of 2000 rpm.

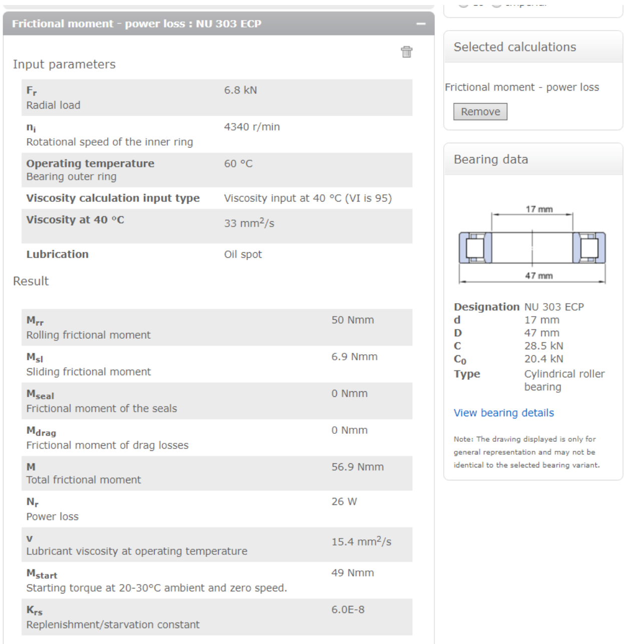

Frictional moment - power loss : NU 303 ECP

Input parameters

F_r Radial load	6.8 kN
n_i Rotational speed of the inner ring	4340 r/min
Operating temperature Bearing outer ring	60 °C
Viscosity calculation input type	Viscosity input at 40 °C (VI is 95)
Viscosity at 40 °C	33 mm²/s
Lubrication	Oil spot

Result

M_{rr} Rolling frictional moment	50 Nmm
M_{sl} Sliding frictional moment	6.9 Nmm
M_{seal} Frictional moment of the seals	0 Nmm
M_{drag} Frictional moment of drag losses	0 Nmm
M Total frictional moment	56.9 Nmm
N_r Power loss	26 W
v Lubricant viscosity at operating temperature	15.4 mm²/s
M_{start} Starting torque at 20-30°C ambient and zero speed.	49 Nmm
K_{rs} Replenishment/starvation constant	6.0E-8

Selected calculations

Frictional moment - power loss

Bearing data

Designation	NU 303 ECP
d	17 mm
D	47 mm
C	28.5 kN
C_0	20.4 kN
Type	Cylindrical roller bearing

View bearing details

Note: The drawing displayed is only for general representation and may not be identical to the selected bearing variant.

Figure 21 NU 303 ECP bearing calculations

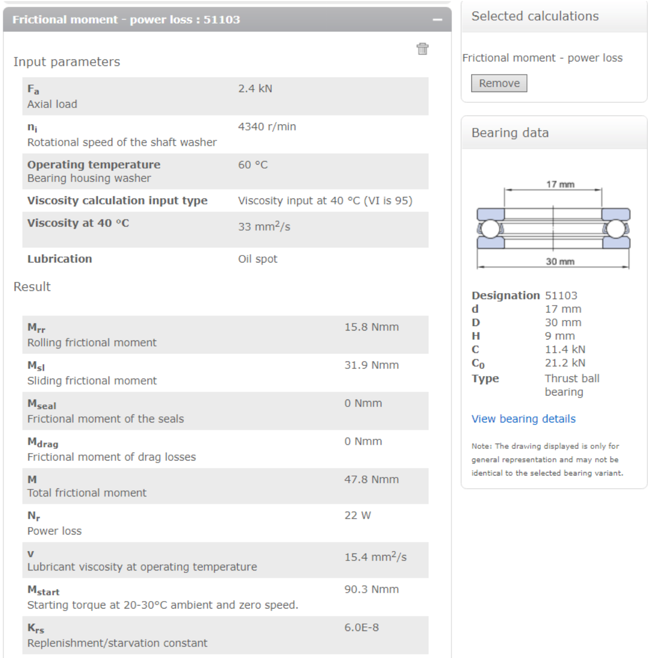

Frictional moment - power loss : 51103

Input parameters

F_a Axial load	2.4 kN
n_i Rotational speed of the shaft washer	4340 r/min
Operating temperature Bearing housing washer	60 °C
Viscosity calculation input type	Viscosity input at 40 °C (VI is 95)
Viscosity at 40 °C	33 mm²/s
Lubrication	Oil spot

Result

M_{rr} Rolling frictional moment	15.8 Nmm
M_{sl} Sliding frictional moment	31.9 Nmm
M_{seal} Frictional moment of the seals	0 Nmm
M_{drag} Frictional moment of drag losses	0 Nmm
M Total frictional moment	47.8 Nmm
N_r Power loss	22 W
v Lubricant viscosity at operating temperature	15.4 mm²/s
M_{start} Starting torque at 20-30°C ambient and zero speed.	90.3 Nmm
K_{rs} Replenishment/starvation constant	6.0E-8

Selected calculations

Frictional moment - power loss

Bearing data

Designation	51103
d	17 mm
D	30 mm
H	9 mm
C	11.4 kN
C_0	21.2 kN
Type	Thrust ball bearing

View bearing details

Note: The drawing displayed is only for general representation and may not be identical to the selected bearing variant.

Figure 22 51103 bearing calculations

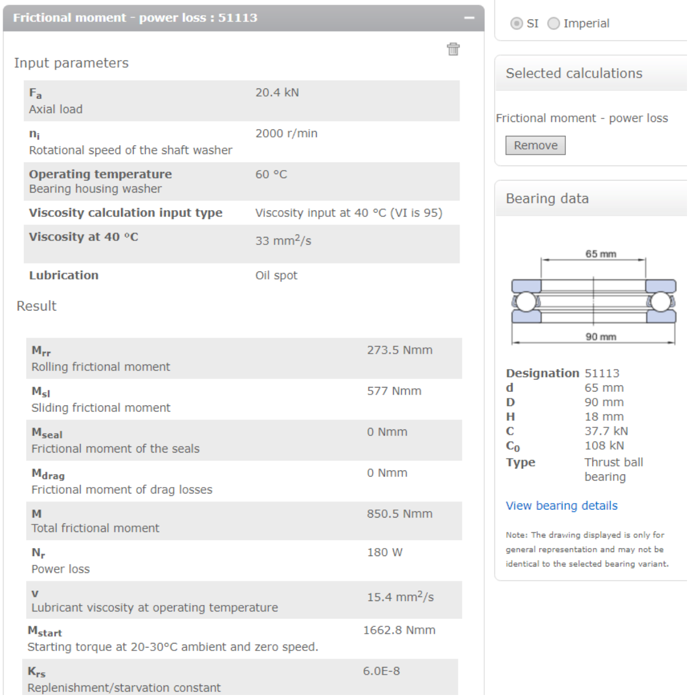

Frictional moment - power loss : 51113

Input parameters

F_a Axial load	20.4 kN
n_i Rotational speed of the shaft washer	2000 r/min
Operating temperature Bearing housing washer	60 °C
Viscosity calculation input type	Viscosity input at 40 °C (VI is 95)
Viscosity at 40 °C	33 mm²/s
Lubrication	Oil spot

Result

M_{rr} Rolling frictional moment	273.5 Nmm
M_{sl} Sliding frictional moment	577 Nmm
M_{seal} Frictional moment of the seals	0 Nmm
M_{drag} Frictional moment of drag losses	0 Nmm
M Total frictional moment	850.5 Nmm
N_r Power loss	180 W
v Lubricant viscosity at operating temperature	15.4 mm²/s
M_{start} Starting torque at 20-30°C ambient and zero speed.	1662.8 Nmm
K_{rs} Replenishment/starvation constant	6.0E-8

Selected calculations

Frictional moment - power loss

Bearing data

Designation	51113
d	65 mm
D	90 mm
H	18 mm
C	37.7 kN
C_0	108 kN
Type	Thrust ball bearing

Note: The drawing displayed is only for general representation and may not be identical to the selected bearing variant.

Figure 23 51113 bearing calculations

Figure 24 presents the bearing losses in Watt of all the clamping related bearings and Figure 25 presents these losses as a percentage of transmitted power.

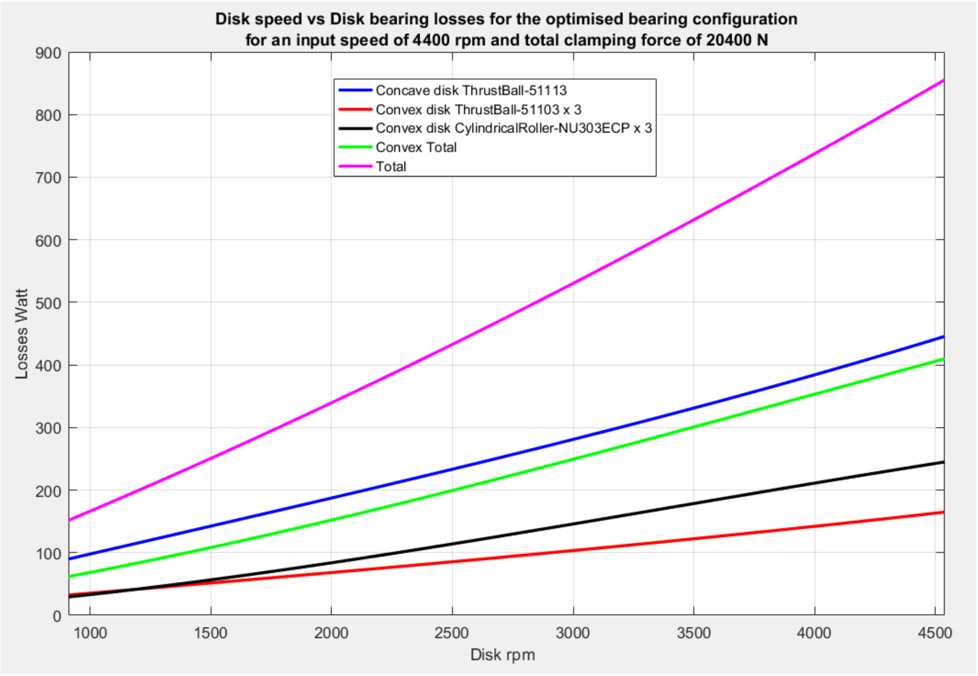

Figure 24 Clamping bearing losses in Watt

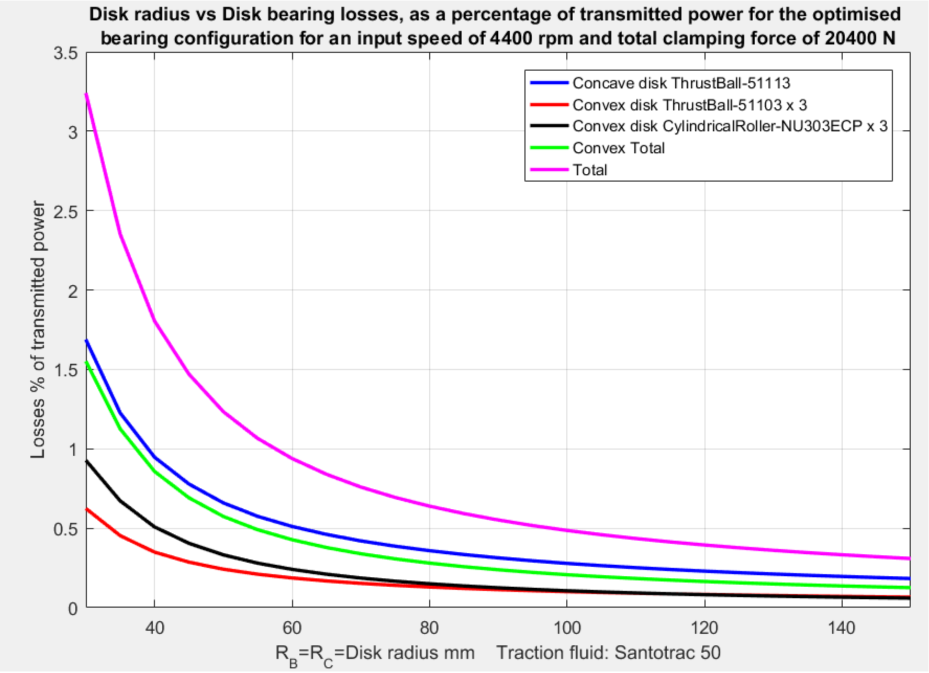

Figure 25 Clamping bearing losses as a % of transmitted power

It can thus be concluded that overall disk/clamping bearing losses, under the influence of the clamping force, is at a maximum of less than 3.5 %. Note that when a smaller ratio range is required, like in the case with AMT integration in section 5.2, only a 3.16 ratio range is required, corresponding to a minimum disk radius of about R_B=R_C=45 mm and according to Figure 25 will reduce the total bearing losses to about 1.5%.

6.1.1 Clamping force advantages

The RADIALcvt configuration includes the following two important clamping force advantages.

- **Clamping force utilization:** As already mentioned in section 5.2, a unit of clamping force supports two parallel friction interfaces, and all other CVT's supports only one, thus in equal conditions the RADIALcvt should have 50% of the clamping bearing losses.
- **Clamping force location:** The RADIALcvt clamping force, bearing losses are only associated with the RADIALcvt output, namely the Convex and Concave disks, while the RADIALcvt input, the radial drivers, are in equilibrium as mentioned in section 4.3.5. Thus these bearing losses, for a given clamping force, are only a function of the RADIALcvt output speed. This has the obvious low loss advantages in low output

speed ratios. In contrast in all other CVT's, the clamping force is associated with both the input and output speeds of the respective CVT, thus for a given clamping force the applicable speed for bearing loss calculation would be the average of the input and output speeds.

6.2 Radial shaft bearing losses

As described in section 4.3.5 the radial shafts experience no radial load as a result of its interaction though the two friction drive contacts as the tangential forces cancel out. Thus the bottom radial bearing experience the radial and axial force created in its 1:1 Zerol bevel drive with the input shaft. Using the equation provided by (TIMKEN, 2017) the tangential force and axial thrust of the Zerol gear is calculated and used as input in the bearing loss calculations. For a total of 70 N.m input torque, resulting in 23.3 N.m per radial shaft, the radial force on the bottom 6003 deep groove ball bearing is 1735 N and the axial force 446 N. Figure 26 presents the losses as calculated by the online SKF bearing calculator. The loss is only 22 Watt per bearing and thus a total of 66 Watt or about 0.2% if 30 kW is transmitted and can thus be ignored for a first prototype analysis. Note that the radial shaft bearing losses are load dependent.

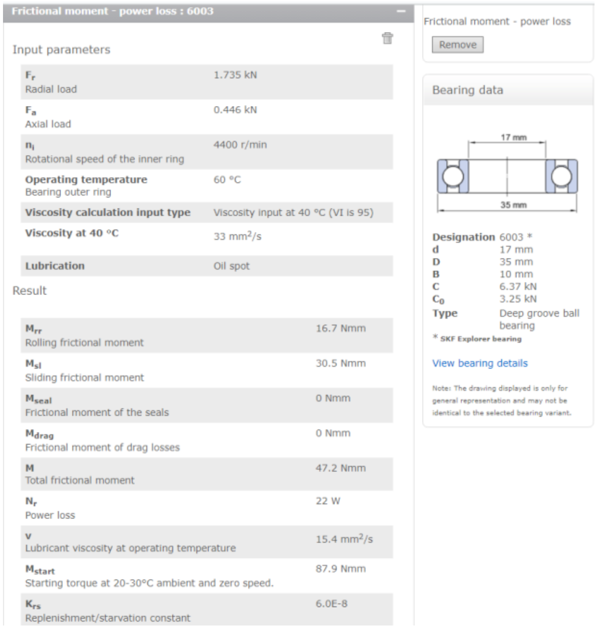

Input parameters

F_r Radial load	1.735 kN
F_a Axial load	0.446 kN
n_i Rotational speed of the inner ring	4400 r/min
Operating temperature Bearing outer ring	60 °C
Viscosity calculation input type	Viscosity input at 40 °C (VI is 95)
Viscosity at 40 °C	33 mm²/s
Lubrication	Oil spot

Result

M_{rr} Rolling frictional moment	16.7 Nmm
M_{sl} Sliding frictional moment	30.5 Nmm
M_{seal} Frictional moment of the seals	0 Nmm
M_{drag} Frictional moment of drag losses	0 Nmm
M Total frictional moment	47.2 Nmm
N_r Power loss	22 W
v Lubricant viscosity at operating temperature	15.4 mm²/s
M_{start} Starting torque at 20-30°C ambient and zero speed.	87.9 Nmm
K_{rs} Replenishment/starvation constant	6.0E-8

Bearing data

Designation	6003 *
d	17 mm
D	35 mm
B	10 mm
C	6.37 kN
C_0	3.25 kN
Type	Deep groove ball bearing

* **SKF Explorer bearing**

Note: The drawing displayed is only for general representation and may not be identical to the selected bearing variant.

Figure 26 Bottom radial driver bearing losses.

7 Ratio shifting analysis

7.1 Geometry analysis

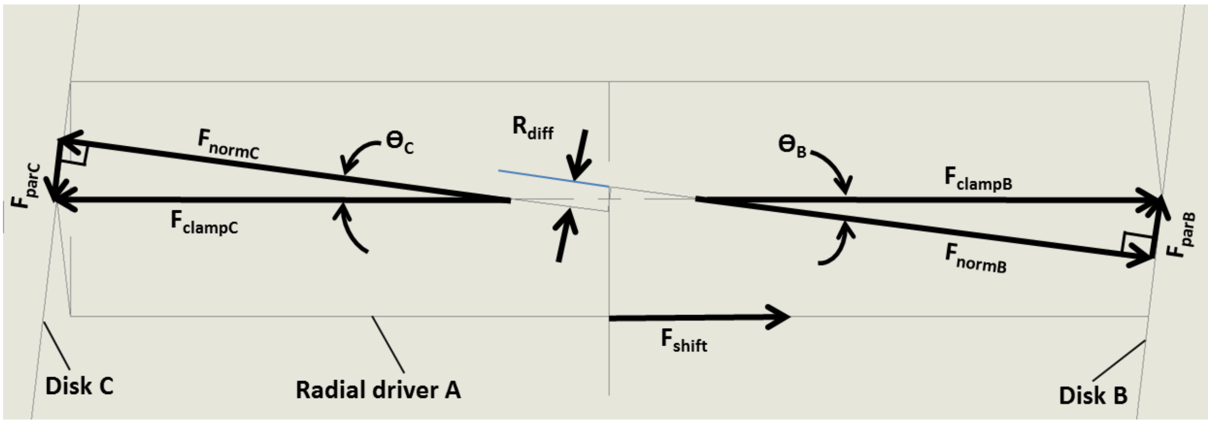

Figure 27 Radial driver force diagram

Figure 27 presents the two force diagrams on the radial driver as a result of the Convex disk (B) and Concave disk (C) being clamped together by a force F_{clampB} which under normal operating conditions is equal to F_{clampC} resulting in line contact between the two disks and the Radial driver. It is assumed that the normal force (F_{parB} and F_{parC}) between the respective disk and Radial driver act at the centre of the contact line. Disk B convex angle is Θ_B and disk C concave angle is Θ_C and is currently taken as being equal.

The force F_{shift} acts perpendicular to the radial driver axis and is the result of moving the radial driver shaft in the direction of F_{shift} during ratio shifting, thus to a larger radius of R_B and R_C.

The following relationships can be established from Figure 20 and above.

$$F_{parB} = (F_{clampB} + F_{shift})\sin(\Theta_B) \qquad \text{(R1)}$$

$$F_{parC} = (F_{clampC} - F_{shift})\sin(\Theta_C) \qquad \text{(R2)}$$

The difference between the vertical components of F_{parB} and F_{parC} provides the resultant force shifting F_S which will be exerted on the radial driver to move it to a different radial ratio position. Thus from above

$$F_s = F_{parB}\cos(\Theta_B) - F_{parC}\cos(\Theta_C) \qquad \text{(R3)}$$

Combining equation 1 to 3 provides

$$F_S = \cos(\Theta_B)(F_{clampB} + F_{shift})\sin(\Theta_B) - \cos(\Theta_C)(F_{clampC} - F_{shift})\sin(\Theta_C) \quad \text{(R4)}$$

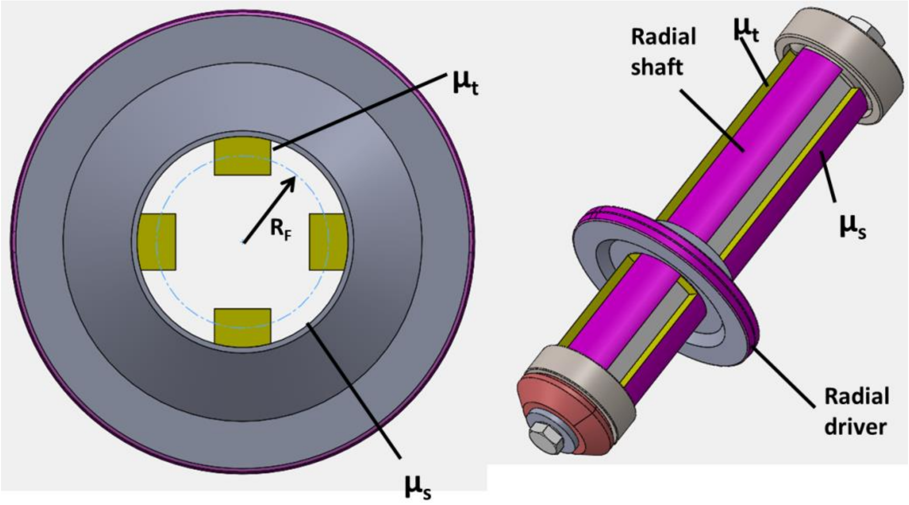

Figure 28 Radial shaft and driver

In order to shift, F_S needs to be larger than F_{fric}, the friction force with friction coefficient μ_t between the radial driver and radial shaft created by the torque T_t being transmitted, added to the friction force with friction coefficient μ_s between the radial driver and radial shaft created by F_{shift}, thus:

$$F_{fric} = T_t \mu_t / R_F + F_{shift} \mu_s \quad \text{(R5)}$$

In order for the current ratio to be in equilibrium, F_S, in equation R4 is set to zero and solving for F_{shift} , while noting that $F_{clamp} = F_{clampB} = F_{clampB}$ =clamping force across disks, gives:

$$F_{shift} = F_{clamp} [\cos(\Theta_C)\sin(\Theta_C) - \cos(\Theta_B)\sin(\Theta_B)]/[\cos(\Theta_B)\sin(\Theta_B) + \cos(\Theta_C)\sin(\Theta_C)] \quad \text{(R6)}$$

From equation R6 is can be seen that F_{shift} is only zero if $\Theta_C=\Theta_B$, thus if they differ F_{shift} will represent the force required to keep the RADIALcvt in the current ratio.

The radial driver also experiences a torque T_D around an axis perpendicular to Figure 27 as a result of the distance R_{diff} and it is calculated by:

$$T_D = 0.5R_{diff}(F_{normB} + F_{normC}) \quad \text{(R7)}$$

In terms of the clamping forces, equation R7 can be written as:

$$T_D=0.5R_{diff}(F_{clampB}\cos(\Theta_B) + F_{clampC}\cos(\Theta_C)) \tag{R8}$$

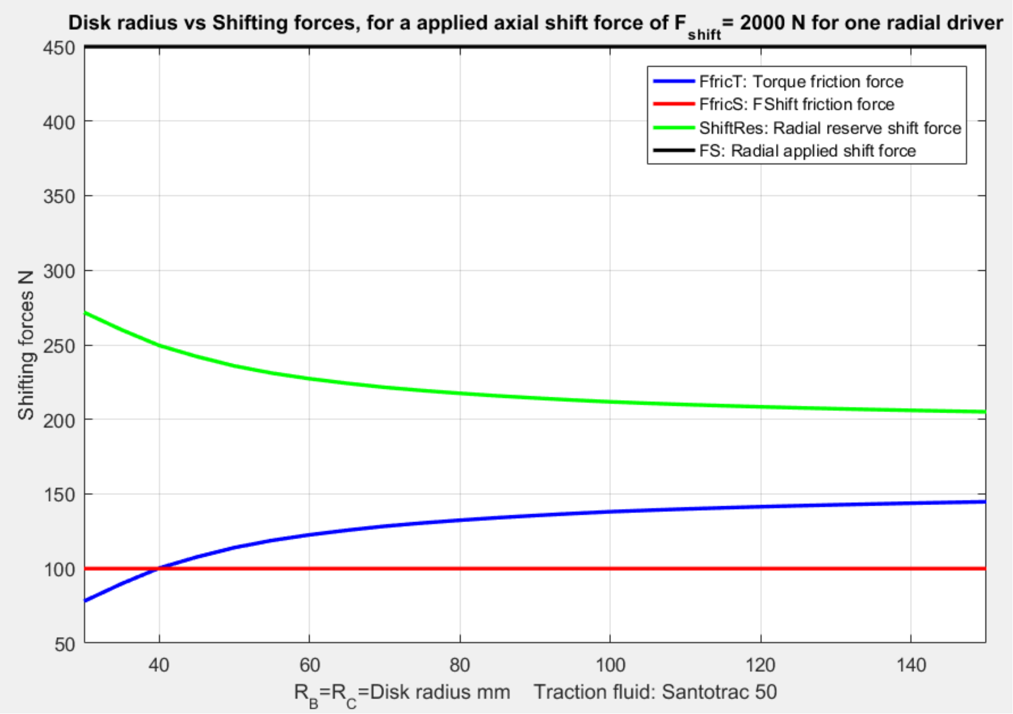

Figure 29 Ratio shifting forces

Figure 29 below present the ratio shifting parameters for the conditions presented in Figure 9 to Figure 14 with μ_t =μ_s=0.05. It can be seen that ShiftRes= F_S- $F_{fric,}$ has positive values thus the shifting force F_{shift}=2000 N will be sufficient to overcame the friction. ShiftRes thus represents the force available to act on the two rolling friction drive contact interfaces, on either side of the radial driver, to move it to a larger radius/values of R_B and R_C. The rate of this radius change will be further investigated when experimental data is available, but should be a function of clamping force and torque transmitted.

The moment T_D as calculated from equation R8 might also have an effect on μ_t and μ_s as it might tend to continually close the tolerance gap between the radial driver and radial shaft on opposite sides in an axial direction of the radial driver and will also be investigated when experimental data is available. Shifting friction force can be drastically reduced by implementing ball splines between the radial shafts and the radial drivers. In this case μ_t and μ_s will represent rolling friction which is much lower than the above values of 0.05 for sliding friction, but the additional cost penalty need to be considered.

7.1.1 Alternative radial shaft and driver design

Figure 24 presents and alternative Radial shaft and Radial driver design in which μ_t is drastically reduced as follows. The Radial shaft is modified to include a Radial slot right through its center including a wider Roller slot at each side. The Radial driver is modified to include a Roller pin, mated at its ends in cavities in the Radial driver and secured by two Securing pins. The Roller pin carries two Rollers that in operation roll along the Roller slots. In this design the Rollers can be of the SKF RSTO type of support rollers (SKF, 1989) with integrated needle rolling bearing. In the Figure 30 design the torque T_t is transmitted via the Rollers and thus in this case μ_t presents rolling friction in the Roller's needle bearing together with the rolling friction of the Rollers in the Roller slots, while in the Figure 28 case μ_t presented sliding friction between two surfaces, thus drastically reducing the value of μ_t in the Figure 30 design and thus reducing F_{fric} as per equation R5. μ_s remains unchanged in this design.

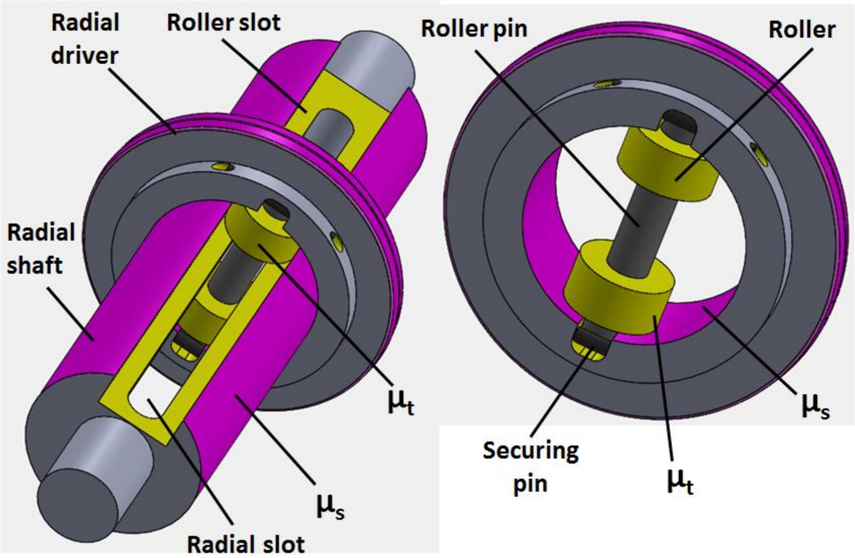

Figure 30 Modified radial shaft and driver design

7.2 Total shifting torque and forces

The total torque V_t on the variator and the ball screw shifting force F_{bs} for the sum of all the radial drivers due to F_{shift} is calculated as follows:

$$V_t = F_{shift}\, n_{rd} L_{ramp}/(2\pi) \qquad \text{(R9)}$$

$$F_{bs} = V_t/R_{bv} \qquad \text{(R10)}$$

Where n_{rd} = number of radial drivers

L_{ramp} = the lead m/rev of the ramps on the casing on which the variator rides

R_{bv} =the radius from the RADIALcvt input axis to the ball screw attachment

Since F_{shift} is constant, V_t= 76 N.m and F_{bs}=381 N are also constant for the conditions in Figure 29. Note that as discussed in section 4.3, the normal force Q (directly related to the clamping force), which currently is constant, need to be varied, for optimization purposes, to allow a near constant input torque T_t. Thus if Q is not constant then F_{shift} will vary accordingly. Above values is only given as an example to present the order of magnitude.

8 Prototype testing

A RADIALcvt prototype was manufactured and Figure 31 presents the main variator components. The prototype was designed according to the parameters in section 2 but capable of up to 100 N.m input torque, limited by the radial shaft Zerol bevel gears.

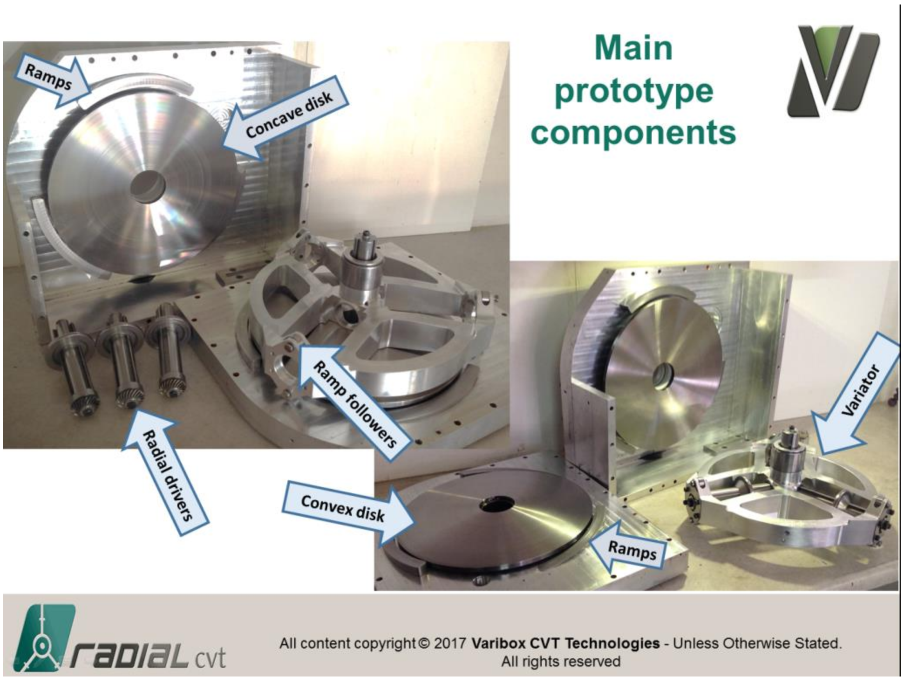

Figure 31 Prototype variator components

The disks were manufactured from EN36B (655M13) steel and case hardened to 60 HRC. It was then hard machined and finished with a diamond burnishing tool to a surface finish of 0.15 um Ra for the convex disk and 0.175 um Ra for the concave disk. These values are within range of required values. See Figure 15. The radial drivers were manufactured from Bohler S600 high speed steel and hardened to 64 HRC.

The first set of tests was performed at the University of the Witwatersrand Johannesburg, South Africa (WITS) on 3 October 2017. The prototype being tested included the variator components in Figure 31 as well as a combining planetary gearing as presented in the exploded view of Figure 32 below.

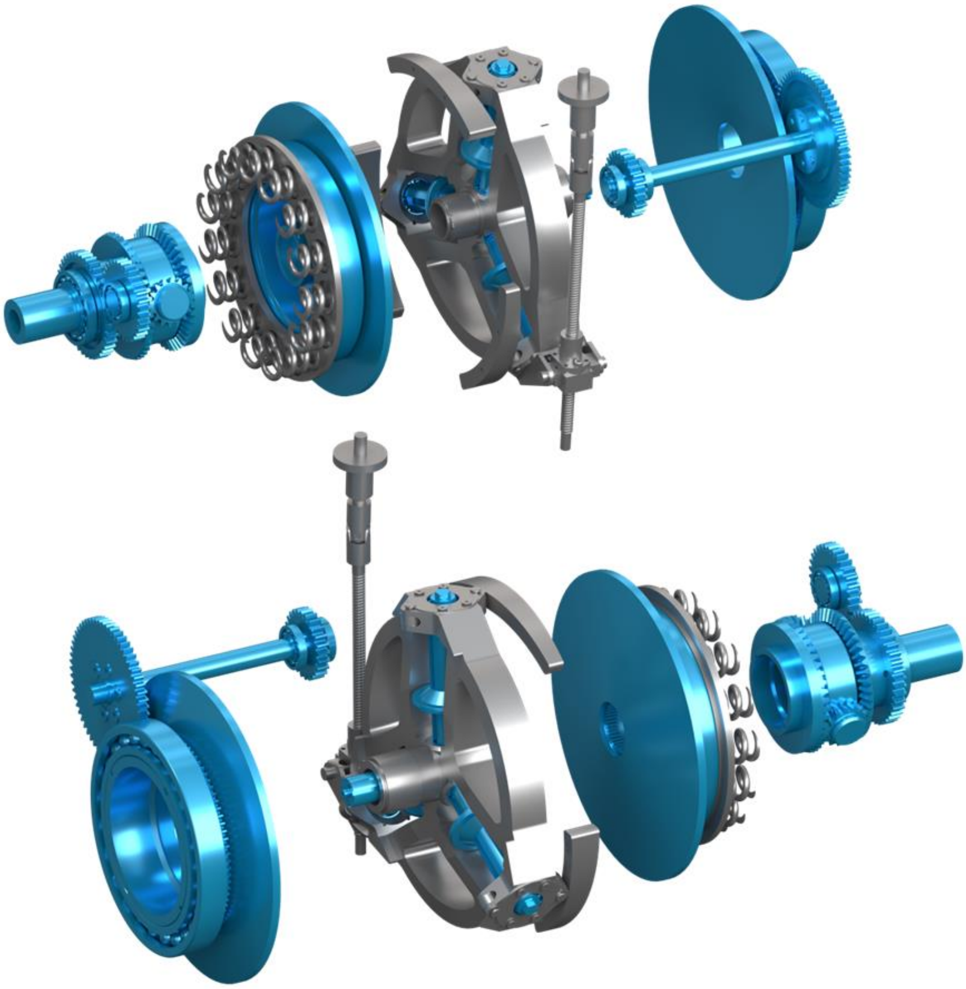

Figure 32 Prototype components including combining planetary gearing

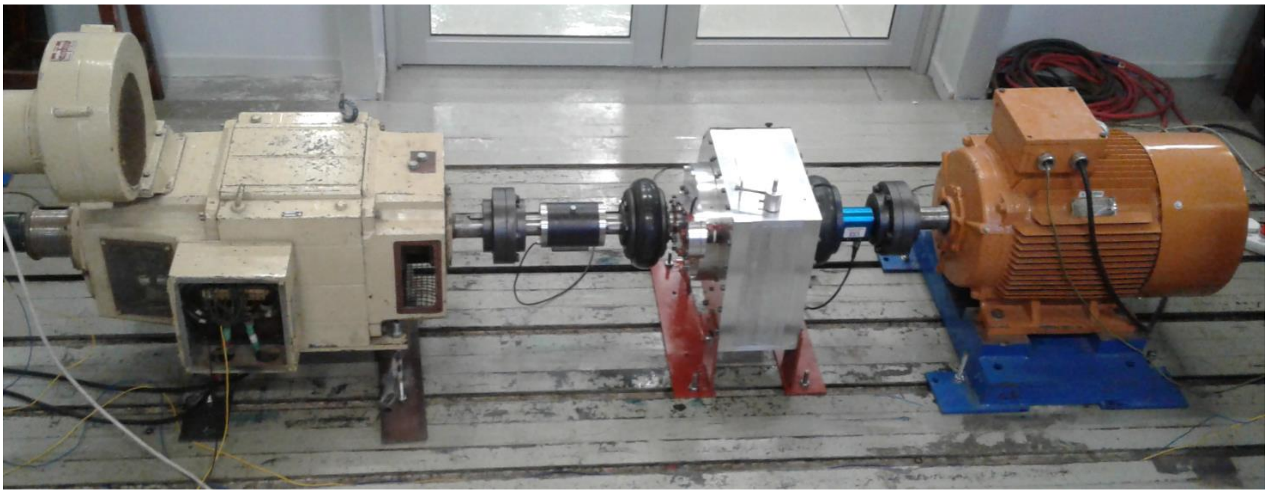

Figure 33 RADIALcvt experimental setup

The test setup is presented in Figure 33 where the (power source) VFD controlled AC motor, on the right, is coupled to an input torque transducer which is coupled to the input of the RADIALcvt. The output of the RADIALcvt is coupled to an output torque transducer which is coupled to a DC motor on the left. The DC motor output is coupled to a resistor bank while its field is adjusted/excited to vary the load.

During testing the input speed and torque as well as output speed and torque were measured at about 1 kHz.

Calibration of the torque transducers was performed by replacing the RADIALcvt with a shaft, in above test setup, to match input and output torque as well as input and output speed.

8.1 Test parameters

- All tests were performed with 50 N.m input torque.
- Three sets of tests were done at input rpm of 1500, 2000 and 3000 respectively.
- For each test set, the ratio range was equally divided in 10 test points. Each test point was logged for about 10 seconds resulting in about 10 000 data points for each test point.
- Temperature during the tests varied from 55 to 71^0 C.
- The traction fluid used was 3.8 litres of Santotrac 50. The resulting oil level in the prototype was 62 mm below the disk centre as presented in Figure 34.
- Each test set included a data log of slowly reducing the ratio from the high ratio to low ratio with no load excitation on the DC motor. To account for the DC motor spinning losses output power were subtracted from input power to result in the spinning losses of the prototype.
- Throughout all tests clamping force were constant at 20400 N.

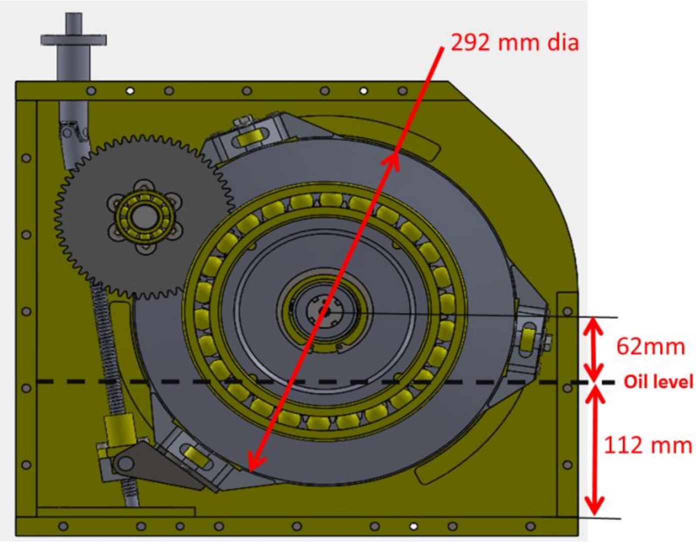

Figure 34 Prototype oil level

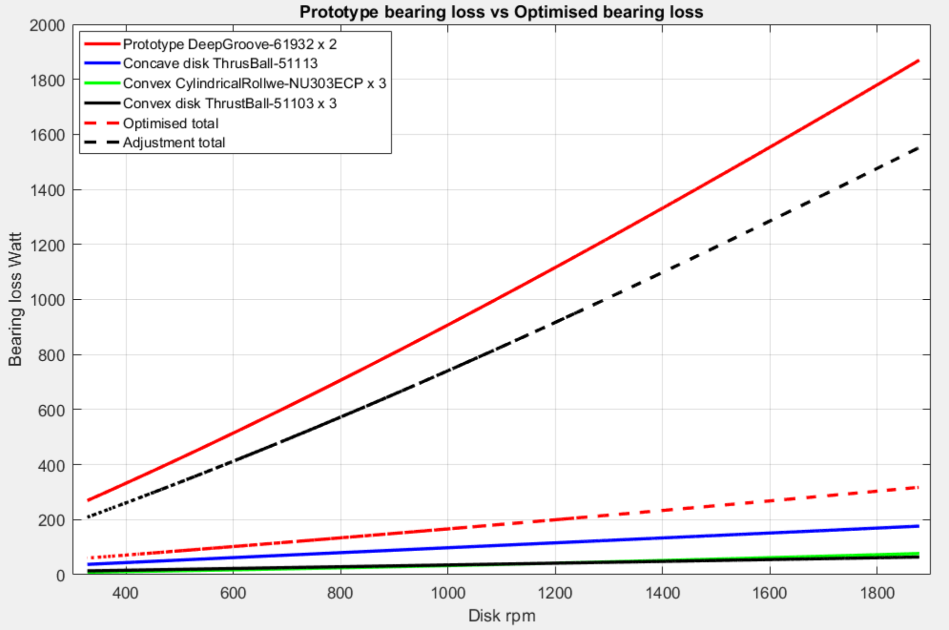

Figure 35 Prototype vs optimised clamping bearing configuration.

- All test results, where applicable, also include the results with the replacement of the 61932 deep groove ball bearings (currently used in the prototype) with the optimised bearing configuration (labelled as “compensated”) of section 6.1 which serve the purpose of acting as the clamping bearings supporting the clamping load. Figure 35 below presents the bearing losses in the prototype bearings vs the losses in the optimised bearing configuration. The losses in Figure 35 were calculated via the online SKF bearing calculator (SKF, SKF) as also presented in section 6.1. A sample calculation for the 61932 bearing is presented in Figure 36.

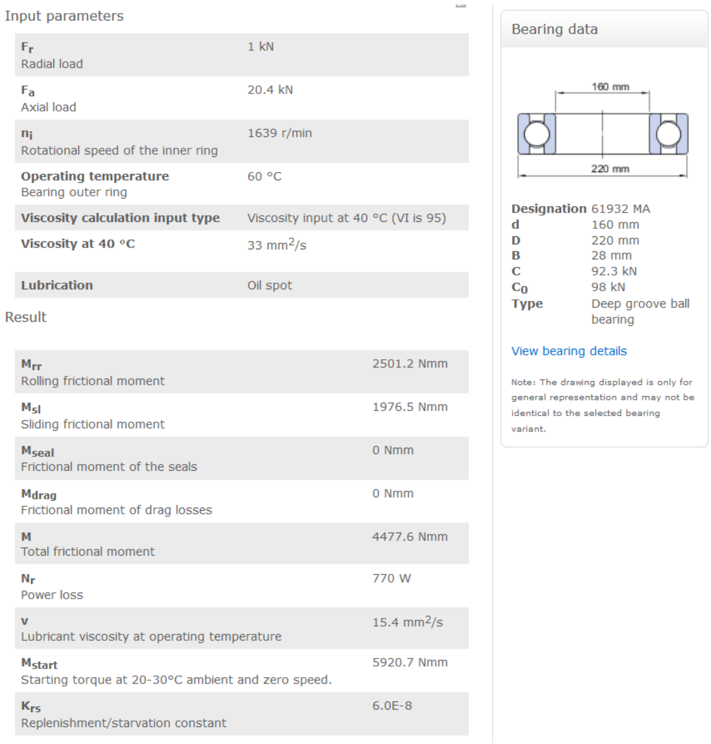

Input parameters

F_r Radial load	1 kN
F_a Axial load	20.4 kN
n_i Rotational speed of the inner ring	1639 r/min
Operating temperature Bearing outer ring	60 °C
Viscosity calculation input type	Viscosity input at 40 °C (VI is 95)
Viscosity at 40 °C	33 mm^2/s
Lubrication	Oil spot

Result

M_{rr} Rolling frictional moment	2501.2 Nmm
M_{sl} Sliding frictional moment	1976.5 Nmm
M_{seal} Frictional moment of the seals	0 Nmm
M_{drag} Frictional moment of drag losses	0 Nmm
M Total frictional moment	4477.6 Nmm
N_r Power loss	770 W
v Lubricant viscosity at operating temperature	15.4 mm^2/s
M_{start} Starting torque at 20-30°C ambient and zero speed.	5920.7 Nmm
K_{rs} Replenishment/starvation constant	6.0E-8

Bearing data

Designation	61932 MA
d	160 mm
D	220 mm
B	28 mm
C	92.3 kN
C_0	98 kN
Type	Deep groove ball bearing

View bearing details

Note: The drawing displayed is only for general representation and may not be identical to the selected bearing variant.

Figure 36 Sample calculation for 61932 bearing.

8.2 No load tests

Figure 37 presents the no load, 100% clamping force, spinning tests for 1500, 2000 and 3000 input rpm respectively together with the optimised bearing configuration compensated results.

Such no load tests, by measuring the power to spin the prototype with no load attached, are very important for the following reason.

The losses in the bearings supporting the clamping forces are included in this measurement. These losses do not change when the transmission is under load conditions and thus load independent in the absence of a loading cam, which is currently the case.

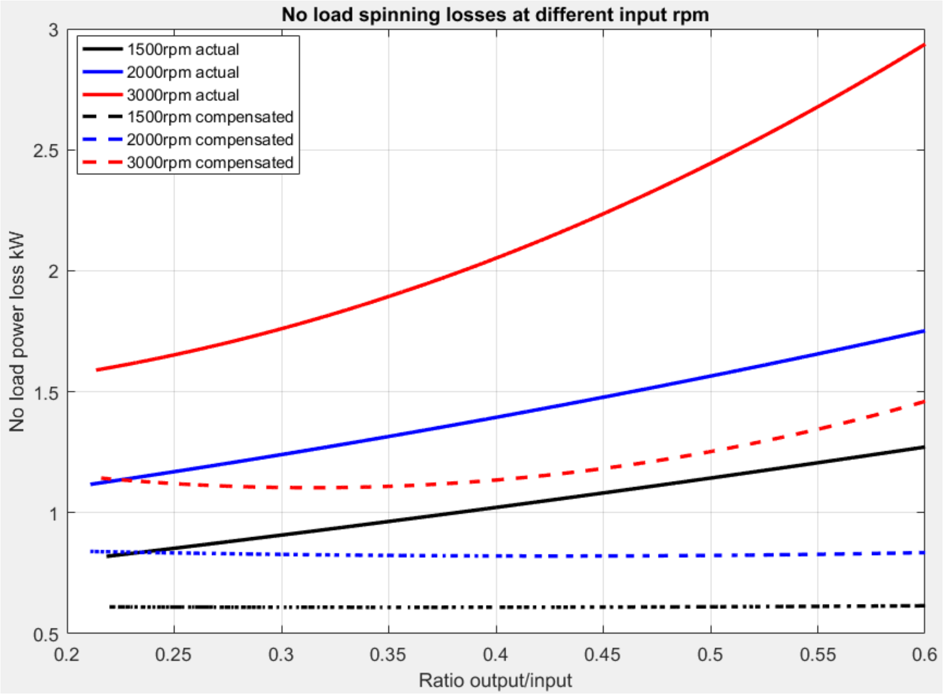

Figure 37 Actual prototype no load spinning test vs optimised clamping bearing configuration (compensated) no load spinning tests.

8.3 Loaded test

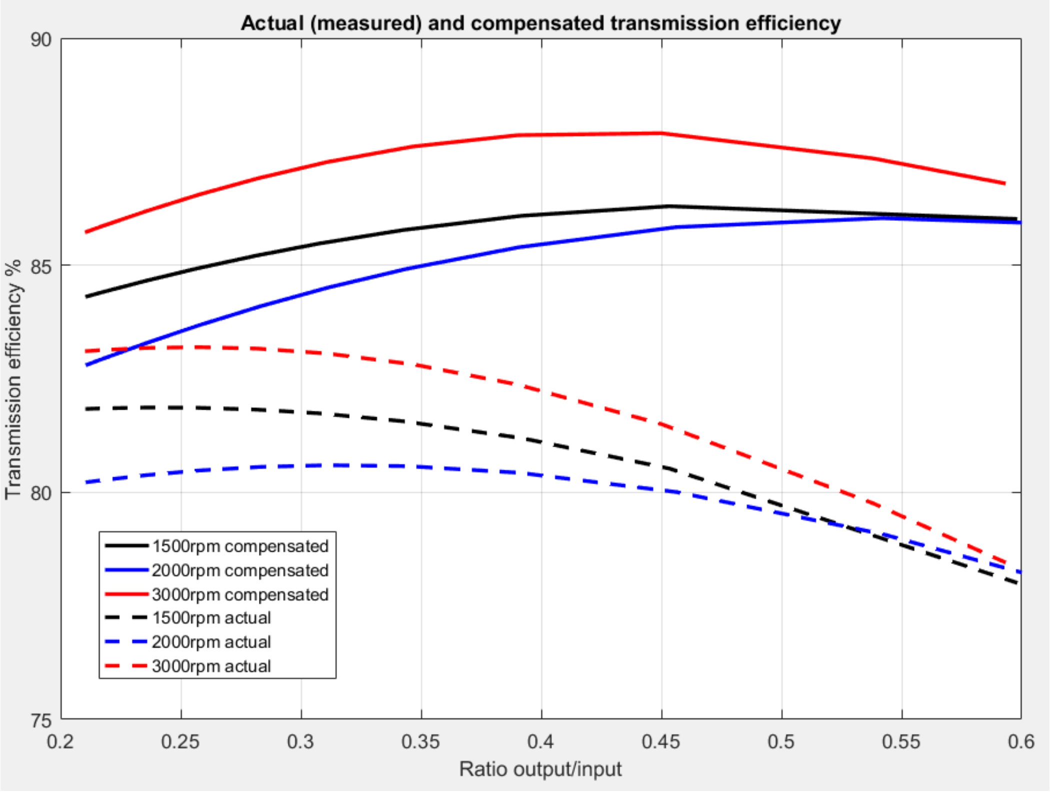

Figure 38 Actual prototype efficiency vs optimised clamping bearing configuration (compensated) efficiency.

Figure 38 include the efficiency results for the loaded tests for an input torque of 50 N.m or about 50% of maximum prototype torque together for the compensated efficiency result, generated by replacing the prototype dep groove ball bearings with the optimised bearing configuration of section 6.1.

8.4 Test result conclusions

The following conclusions and observations can be made:

1. Above results clearly demonstrate the huge advantage of the RADIALcvt in comparison to other commercial CVT's in that the clamping force related bearing losses are only associated with the variator output (disk) speed while in commercial CVT it is associated with the input and output speeds. See also section 6 for a discussion.
2. The no load losses have a more or less linear relationship with the output (disk) speed.
3. Note that 100% clamping force are maintained at all times eliminating a hydraulic control system as well as a loading cam. Commercial CVT's include both a hydraulic control system and loading cam.
4. Referring to Figure 37, if an input torque of 100 N.m is applied to the prototype and input speed is at 3000 rpm, the prototype will transmit 31.4 kW and the compensated spinning losses would amount to 1.15 kW (low ratio) to 1.45 kW(high ratio) or 3.6% to 4.6% of transmitted power respectively. These losses include both the clamping bearing losses, traction no load losses as well as oil churning losses. Especially the oil churning losses should be further investigated in future work.
5. The replacement of the 61932 deep groove ball bearings with the optimised bearing configuration is a must, since deep groove ball bearings in general have very high losses when loaded axially. These bearings were used in the prototype for simplicity as the purpose of the first prototype was mainly to test the ratio shifting mechanism and to serve as a proof of concept.
6. During testing ratio adjustment was done manually. The ratio was easily adjusted and did not present any problems. In future the torque to adjust the ratio will also be measured. At this stage it seems that the lubricated, hardened polished steel on

steel interface between the radial driver inner and radial shafts provides a low enough coefficient of friction to allow for smooth ratio shifting. For the time being it is therefore concluded that the use of ball splines or the alternative Radial shaft and Radial driver design as presented in section 7.1.1 will not be needed and the current low cost solution will be used.

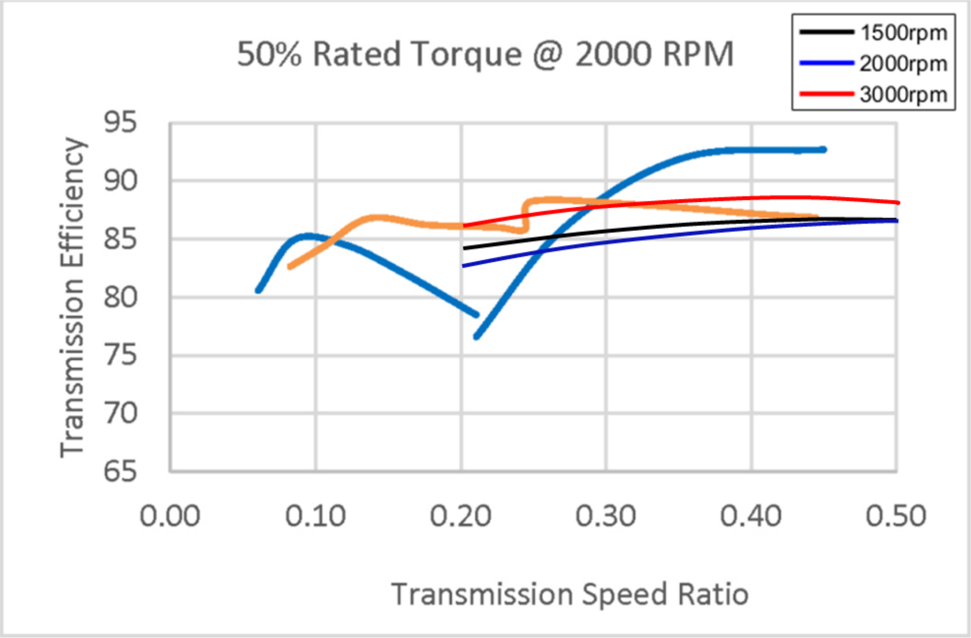

Figure 11. Comparison of Over All Transmission Efficiency.

<u>Figure 39 RADIALcvt efficiency superimposed on the results from (McIndoe G. V., 2016)</u>

7. The RADIALcvt loaded efficiency results of Figure 38 are in line with recently published results of a current in production CVT vs the Dana Variglide CVT (McIndoe G. V., 2016) (as presented in section 11, Figure 63). This is very encouraging for further RADIALcvt development, since the current RADIALcvt results are that of a first prototype while both the current production CVT and Dana Variglide have been in development for many years. As the simulation results of section 4 indicate as well as the fundamental advantages of the RADIALcvt, there is a lot of potential efficiency improvement still to be unlocked in the RADIALcvt configuration. Figure 39 presents the RADIALcvt efficiency of Figure 38 superimposed on the results from (McIndoe G. V., 2016). The orange line represents the production CVT, the light blue line the VariGlide and the red, black and darker blue lines the RADIALcvt efficiency. Note that the RADIALcvt ratio range extends up to 0.6 to the right of Figure 39. Also

note that the RADIALcvt result presents one mode of operation while the production CVT and VariGlide presents two modes.

8. Above is supported by the number of fundamental advantages of the RADIALcvt, as presented in this document, which sets it apart from all other developmental and commercial CVT's.
9. These tests also prove that all the drivers run at the same diameter and that the ratio shifting mechanism operates successfully.

8.5 Future work

The following work will be considered in future testing and development.

1. Test current prototype up to 100 N.m input torque
2. Measure ratio shifting torque and power.
3. Adjust oil level and test no load spinning losses.
4. Implement optimised bearing configuration
5. Investigate/analyse oil drag on the disks. Investigate the use of a dry sump, about 30 Watt oil pump driven, low pressure (1 bar) nozzles system supplying oil to the disk-driver traction drive interface. Video material of the disks during testing showed a lot of oil churning especially at 3000 rpm input in high ratio.
6. Implement drivers with about 5mm of contact length and increased clamping force (in line with section 4.3.4) and test.

9 RADIALcvt E^2 configuration

In a typical RADIALcvt with 2 speed AMT integrated, as presented in section 4.3.3, the RADIALcvt variator will need to shift through its ratio range when the AMT changes speed, which will lead to a power interruption and require some additional control. In order to address above issue the integration of the RADIALcvt into the so-called E^2 transmission configuration was investigated. A typical E^2 transmission configuration includes a variator with a ratio range of say R_L to R_H. In the First mode the E^2 transmission vary its ratio while the variator shifts from R_L to R_H. In this First mode of operation the input of the E2 transmission is coupled to the input of the variator and the output of the E^2 transmission is coupled to the output of the variator. When R_H is reached, the E^2 transmission shifts to its Second mode as follows:

The input of the E^2 transmission is coupled to the output of the variator and the output of the E^2 transmission is coupled to the input of the variator. By choosing the correct gearing, above can be accomplish by dog clutches shifting across components with the same rotating speeds while the overall ratio (E^2 transmission input versus output) stays constant.

After the E^2 transmission is shifted to the Second mode of operation, the variator can now adjust its ratio from R_H to R_L to complete the overall ratio range. Thus the lowers overall ratio (E^2 transmission input versus output) is created with the variator in R_L and First mode selected, while the highest overall ratio is created with the variator also in R_L but with Second mode selected.

Note that the variator does not change its ratio when the E^2 transmission changes from the First mode to the Second mode and therefore eliminates the above issues related to 2 speed AMT integration while still having the effect of providing an overall ratio range of (variator ratio range)^2. Thus if the variator ratio range is 3.16 the overall ratio range of the E^2 transmission will be $3.16^2=10$.

Figure 40 and Figure 41 represents the RADIALcvt, modified to serve as an E^2 transmission. Note that all components in yellow, going forward, refers to bearings, bushes, washers and springs. The E^2 transmission input, referred to as the E2 input and in colour green, coupled to the power source, extends through the E^2 transmission while the RADIALcvt input consists of a hollow shaft, in black, around the E2 input, driving the Radial shafts and drivers, also in black. The Radial drivers, drive the Convex and Concave disk, while the disks are coupled to the Combining planetary system via the magenta coloured gearing. The Combining planetary system cage, that serves as the RADIALcvt output, in light blue colour, is in the form of a hollow shaft around the RADIALcvt input. The Combining planetary system includes a configuration, as typically found in automotive differentials, including two bevel gears, coupled to the two disks (directly with the Convex disk and via gearing to the Concave disk), with the bevel gears meshing with the spider bevel gears whose shafts are attached to the Combining planetary system cage, which serves as the output of the

RADIALcvt. Above components function according to the description of the RADIALcvt in PCT patent application WO2017/143363 (Naude, 2017).

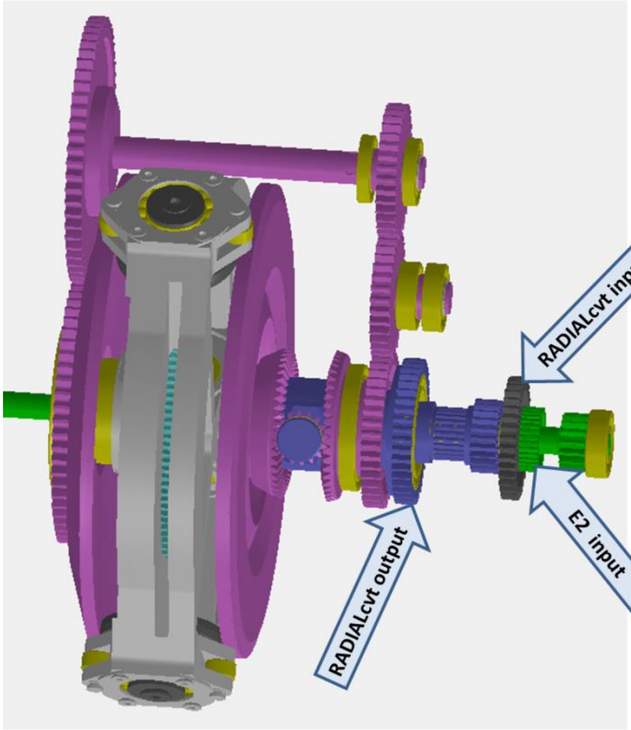

Figure 40 RADIALcvt in E2 configuration

Note that the bevel gears attached to the RADIALcvt input shaft mates with the bevel gears attached to the Radial shafts from the right of Figure 41 and thus the E2 input, RADIALcvt output and input all rotate in the same direction.

The gear ratio of the gears in magenta colour in Figure 41, coupling the Concave disk to the Combining planetary system can be chosen as such to compensate for the difference in torque capacity between the Convex and Cave disk as presented in section 4.

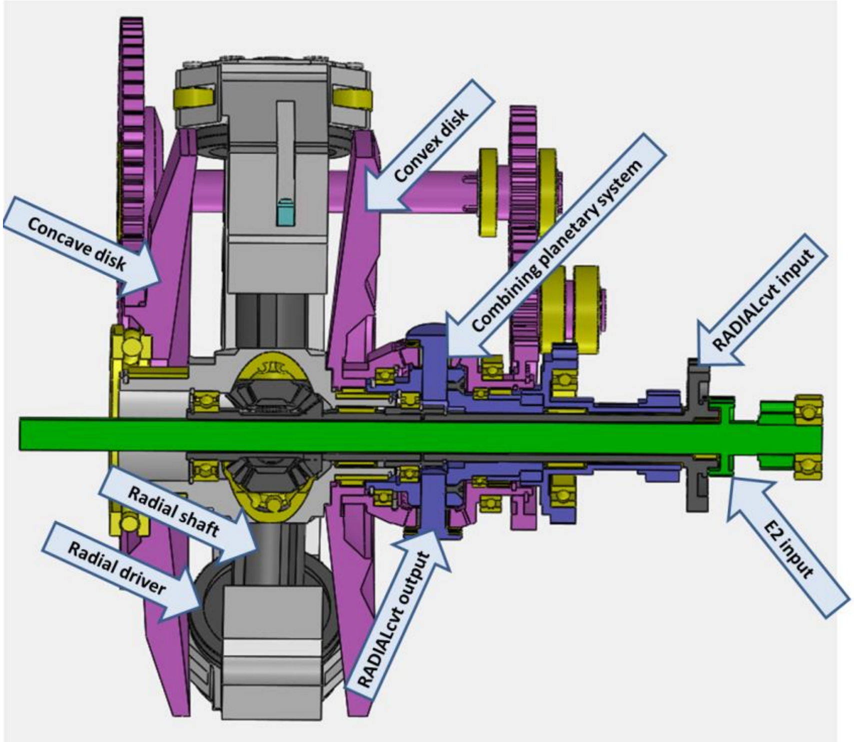

Figure 41 Sectional view of RADIALcvt in E2 configuration

Figure 42 presents the introduction of an Intermediate shaft to realise the two modes of the E^2 transmission. The ratios of the meshing gears are indicated, assuming the gears on the Intermediate shaft are driven. Figure 43 presents a sectional view of the right part of Figure 42. By introducing the Intermediate shaft, the RADIALcvt output is extended via a shaft attached to two meshing gear pairs (light blue components) to the RADIALcvt extended output gear next to dog clutch A (red) on the E2 input shaft. The Intermediate shaft also includes a freely rotatable hollow shaft, which serves as the E^2 transmission output, referred to as E2 output with a gear in the middle and a Dog clutch B and C (red) on either side. The RADIALcvt input is extended to the RADIALcvt extended input gear (black components), which is freely rotatable around the Intermediate shaft. In Figure 38 above all the Dog clutches are in the neutral position and does no coupled the E2 input or E2 output to any other components. All dog clutches are similar to the dog clutches found in for example manual and automated manual transmissions.

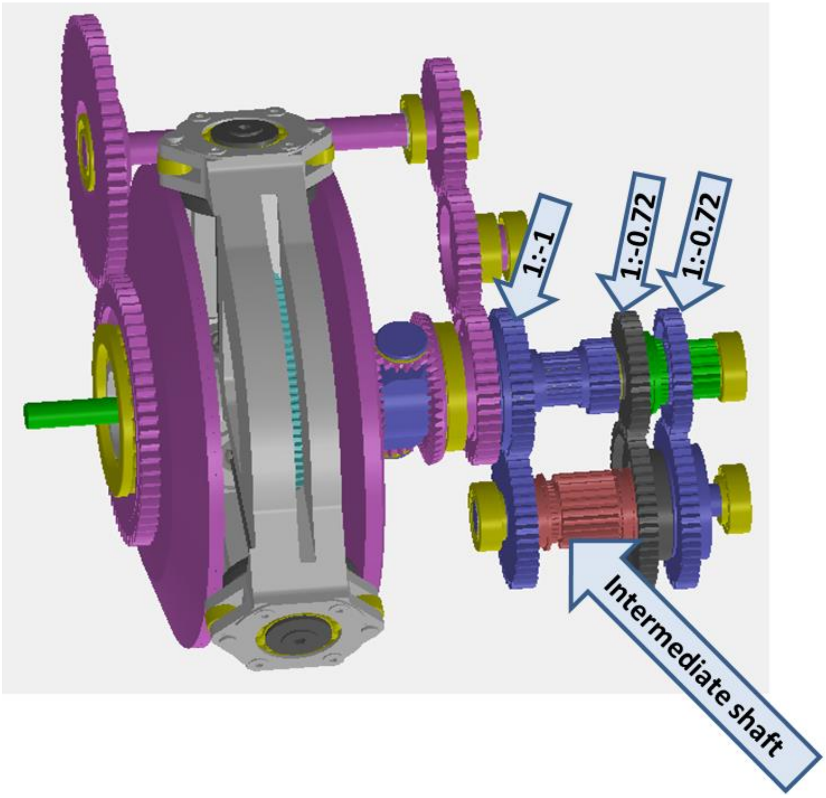

Figure 42 Introduction of an Intermediate shaft

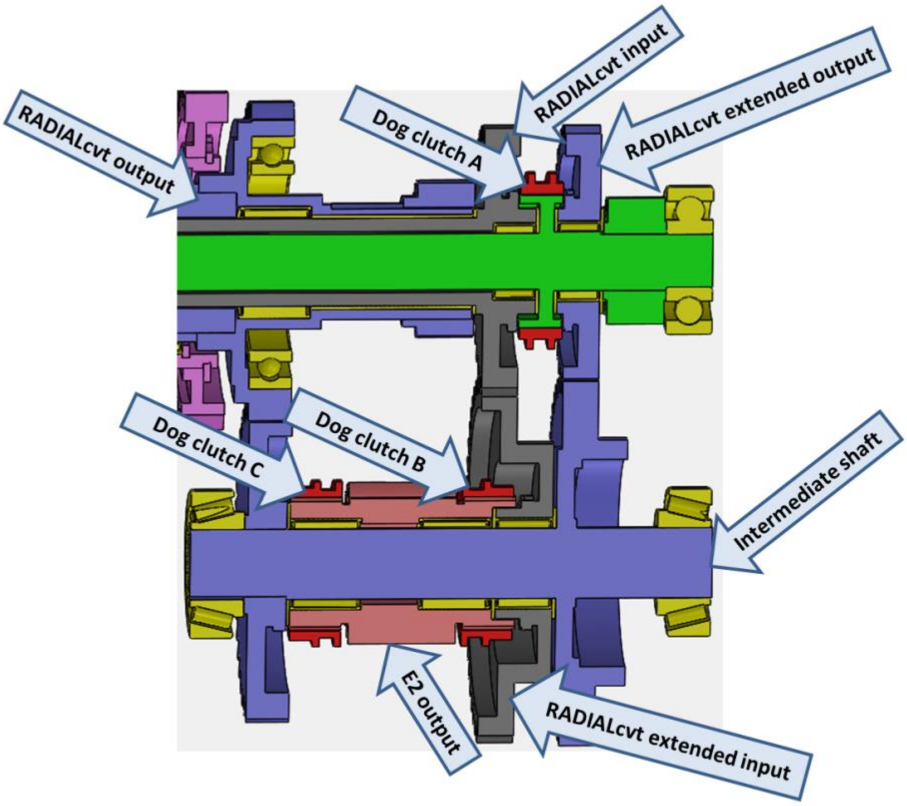

Figure 43 Cross section of Intermediate shaft integration

9.1 First mode of operation

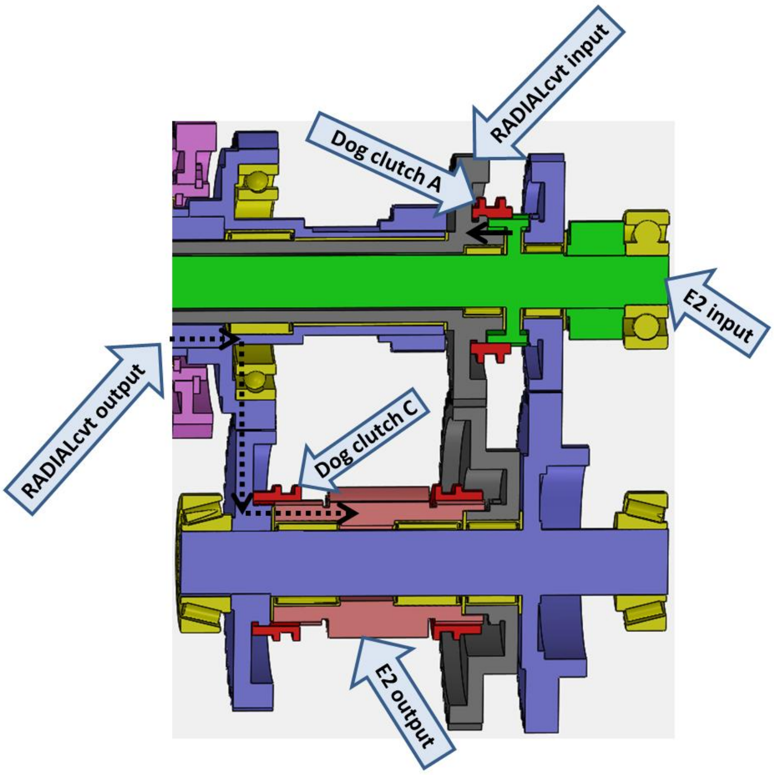

Figure 44 First mode of operation

In the First model of operation, Dog clutch A is shifted to the left in Figure 43 , as presented in Figure 44, and couples the E2 input to the RADIALcvt input in a 1:1 ratio. Dog clutch C is shifted to the left to couple the E2 output to the RADIALcvt output in a 1:-1 ratio. The solid black arrow indicate power flow from the E2 input to RADIALcvt input and the dashed black arrow power flow from the RADIALcvt output to the E2 output. In this First mode the RADIALcvt can shift from its lowest ratio at pull away (largest Radial driver radius on the disks) to its highest ratio (smallest Radial driver radius on the disks).

When the RADIALcvt reached its highest ratio the Second mode of operation, described below, is engaged.

9.2 Second mode of operation

Dog clutch A is shifted to the far right to couple the E2 input to the RADIALcvt extended output. Dog clutch C in shifted to the neutral position and Dog clutch B is shifted to the right to couple the E2 output to the RADIALcvt extended input. Figure 45 presents the power flow after above Second mode selection.

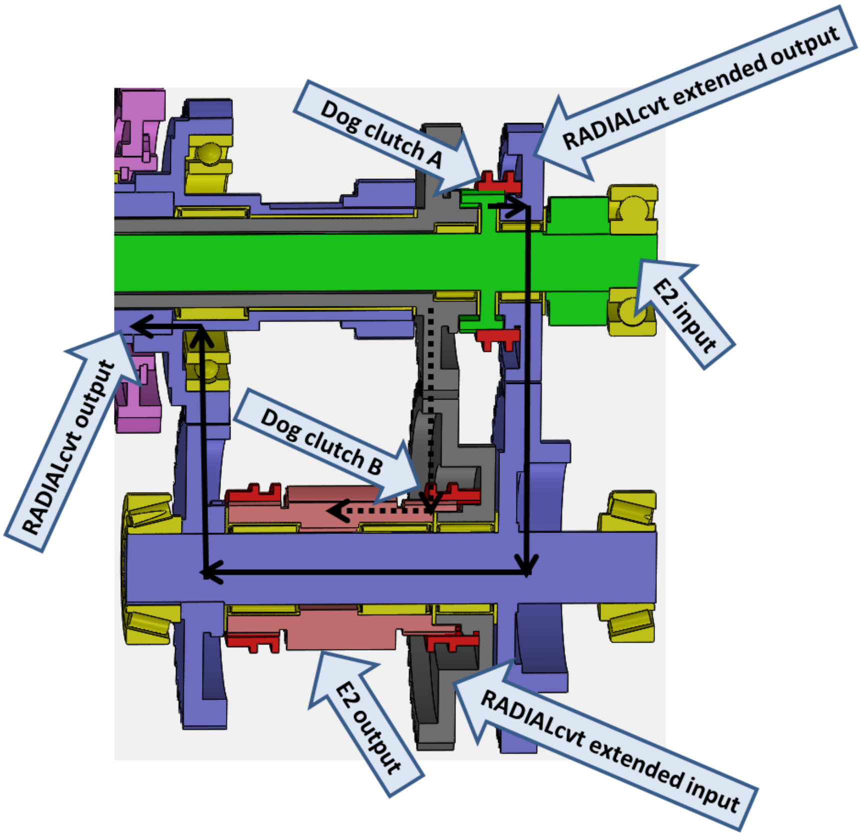

Figure 45 Second mode of operation

In the Second mode operation power thus flows from the E2 input to the RADIALcvt output (solid black arrows) , to the RADIALcvt input and then to the E2 output(dashed black arrows). The RADIALcvt can now continue to shift to its lower ratio to complete the E^2 transmission ratio range.

9.3 First to Second mode synchronization

Assuming a RADIALcvt ratio range of 1:0.23 to 1:0.72 (ratio range 3.16) measured at the RADIALcvt input versus the RADIALcvt output. Also assume the E2 input is rotating at a positive (clockwise, viewed from the RADIALcvt direction) constant 3000 rpm. With the RADIALcvt in its highest ratio and the E^2 transmission in the First mode of operation the speed of the following are calculated:

RADIALcvt output=E2 input x RADIALcvt ratio = 3000 x 0.72 = 2160 rpm

RADIALcvt extended output=RADIALcvt output x (-1) / (-0.72) = 3000 rpm

E2 output = RADIALcvt output x (-1) = -2160 rpm

RADIALcvt extended input = RADIALcvt input x (-0.72) = 3000 x (-0.72) =-2160 rpm

From above it can be seen that the E2 input and RADIALcvt extended output are both rotating at 3000 rpm. Therefore in shifting from the First to Second mode, Dog clutch A will couple E2 input and the RADIALcvt extended output which are already rotating at the same speed. Therefore no speed synchronisation is needed as for example in a manual or automated manual transmission.

Similarly, E2 output and RADIALcvt extended input are also rotating at the same speed (2160 rpm), thus in shifting from the First to Second mode Dog clutch B can couple E2 output and RADIALcvt extended input without any speed synchronisation.

Due to above the shifting of the respective dog clutches, shifting from First to Second mode of operation can be done extremely fast if compared to for example the dog clutch shifting in automated manual and dual clutch transmissions in which speed synchronisation is needed and where the components are not rotating at the same speed.

It should also be noted that the overall ratio (E2 input / E2output) remains constant when shifting from First to Second mode. In all stepped transmission this is not the case.

Also note that the various ratios mentioned can be optimised for different applications. Above is only given to serve as an example.

Also note that all gears used are presented as spur and straight bevel gears and is only used as examples. They may be changed for helical, spiral bevel and Zerol gears to suite specific applications.

9.4 Hard geared low ratio

Launch control in commercial CVT’s presents a challenge as initial launch torque might exceed the maximum traction coefficient and can cause slip and damage in the traction drive components. An example of such a launch situation is pulling away over a kerb. The E^2 transmission allows for easy integration of such a hard geared low ratio feature, which bypasses the variator, as also described in PCT patent application WO2017/143363 (Naude, 2017).

Figure 46 presents the introduction of an idler Low ratio gear freely rotatable on the Intermitted shaft and which is coupled to the gear meshing with the RADIALcvt extended output via a Sprag or one-way clutch and which is driven by a gear on the E2 input shaft by a 1:-0.24 ratio which is fractionally higher in magnitude than the low ratio (0.23) of the RADIALcvt.

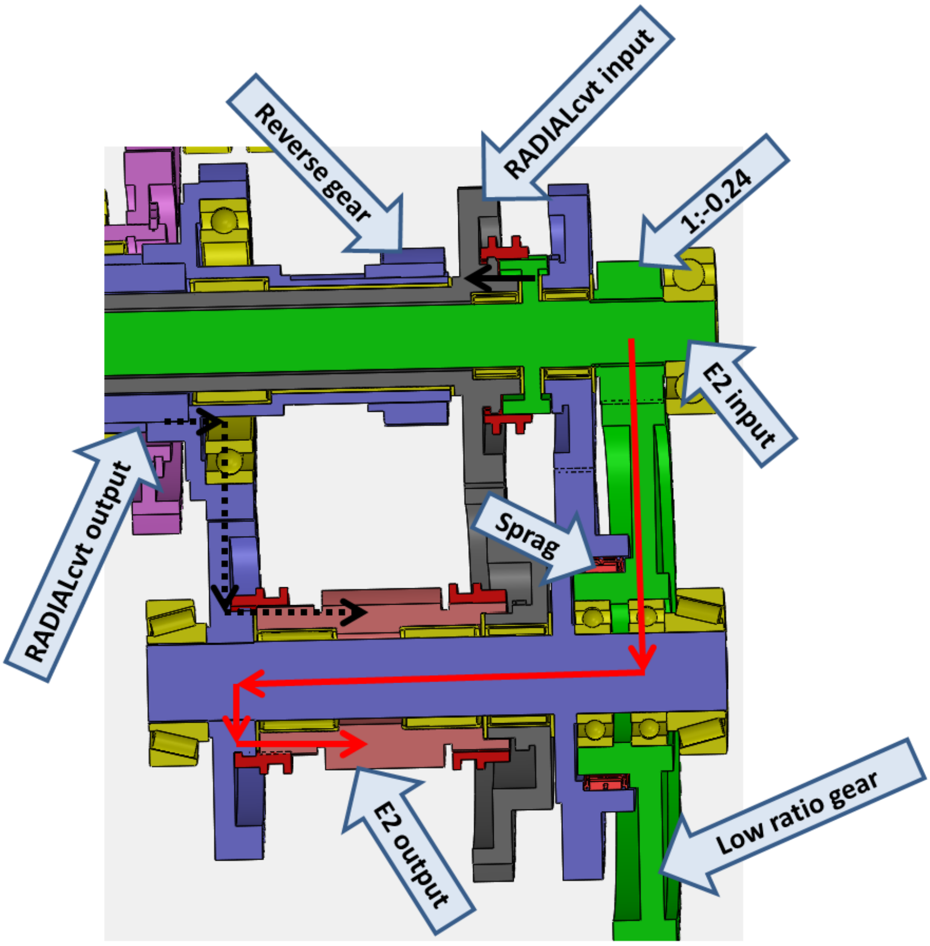

Figure 46 Hard geared low gear integration

Whenever the RADIALcvt is in a ratio lower than 1:0.24, the Low ratio gear will tend to turn faster than the gear it is coupled to via the Sprag and the Sprag will lock. With the Sprag locked the power will flow via the red arrows in Figure 46 from the E2 input to E2 output and therefore bypasses the RADIALcvt. The normal power path of the First mode, shown in black dashed arrows will thus not be active. When the RADIALcvt ratio is above 1:0.24 the Sprag will unlock and the black dashed power path through the RADIALcvt will be active while the red power path will be inactive. Above provides a hard geared ratio for pull away conditions by the addition of minimal components. With no limitation on the launch torque (as is the case with manual transmissions), automatic clutch control will be much easier.

9.5 Hard geared reverse mode

In order to generate reverse in the E^2 transmission, the Low ratio gear and Sprag are utilised in the following way to generate a hard geared reverse, also bypassing the RADIALcvt, with the same pull away benefits as the Hard geared low ratio described in section 9.4

As presented in Figure 47 the RADIALcvt output includes a splined hollow shaft extension on which a Reverse gear with mating splines, being axially slidable, is located (see Figure 46). In order to realise reverse, a Reverse idler gear is introduced, which meshes with the E2 output gear. In order to select reverse, all the Dog clutches A to C are put in the neutral position (their position in Figure 43) and the Reverse gear is slided from its position in Figure 46, to the left to its position in Figure 47 where it engages and meshes with the Reverse idler gear. The red arrows present the power flow during reverse engagement. Reverse drive thus utilises the Hard geared low ratio gearing as well as the RADIALcvt extended output gearing.

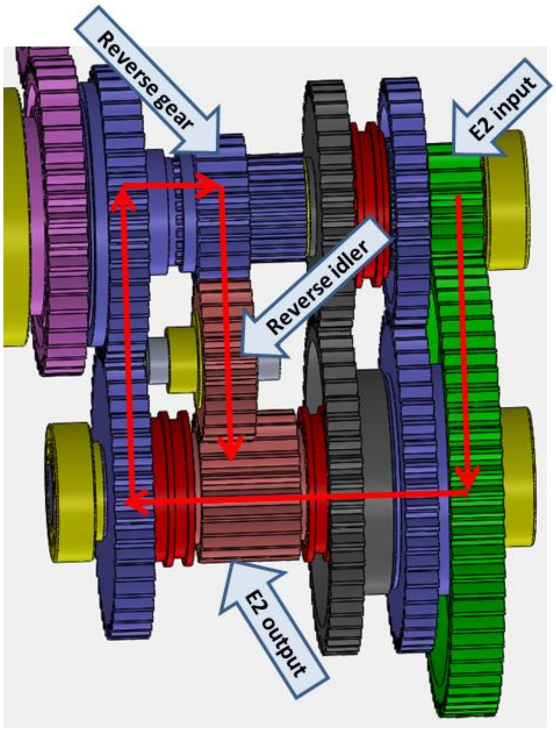

Figure 47 Hard geared reverse

Note that all the components on the Intermediate shaft always rotate in the same direction, except when reverse is engaged and the E2 output rotates in the opposite direction.Also note that above configuration provides a Hard geared reverse selection only, with no variable reverse ratio via the RADIALcvt.

If a variable reverse ratio, with ratio range equal to the First mode is desired, Dog clutch A need to be shifted to the left to couple the E2 input to the RADIALcvt input. Such a configuration would provide for a hard geared reverse for pull away purposes as well as a variable reverse ratio via the RADIALcvt, in the same way as the functioning of the Hard geared low ratio.

9.6 Mode selection mechanism

Mode selection in the E^2 transmission is done via selector forks operating Dog clutches A to C as well as Reverse gear. The selector forks are similar to those found in manual and automated manual transmissions.

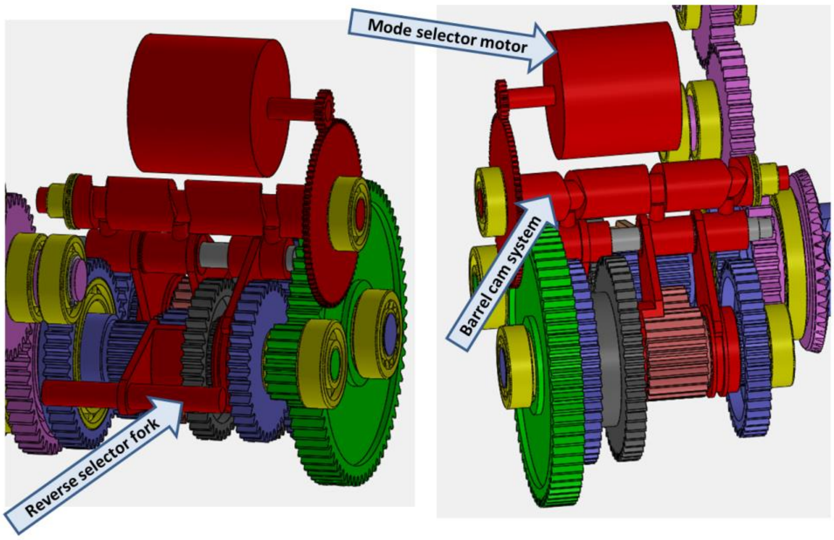

Figure 48 Mode selector mechanism

The Dog clutch A to C selector forks are actuated via a Barrel cam system while Reverse selector fork is driver operated. Figure 48 presents the introduction of the selector forks and Barrel cam system. The Barrel cam system is gear driven by a position controlled Mode selector motor. By rotating the Barrel cam system the selector forks are positioned to an all

Neutral position, First mode position, Second mode position and Reverse position. The Barrel cam system is similar to those found in motorcycle transmissions.

9.7 RADIALcvt ratio actuation and loading cam

In the RADIALcvt functioning, the Variator structure, housing the Radial shafts and drivers, are rotatable around its axis when adjusting the ratio as fully explained in PCT patent application number WO2017/143363 (Naude, 2017). Because the RADIAL drivers make traction drive contact on both sides with the opposite rotating Convex and Concave disks and because the traction drive tangential forces are in opposite directions and of very similar magnitude, as described in section 7, the tangential forces largely cancel out. The result of this is that the torque on the Variator structure is a function of the RADIALcvt input shaft torque. Because the RADIAL drive radius is constant and does not change as the RADIALcvt ratio is changed, the tangential traction drive forces are directly related to the RADIALcvt input torque. Assuming a constant traction coefficient for the moment, then the clamping force will be directly related to the RADIALcvt input torque.

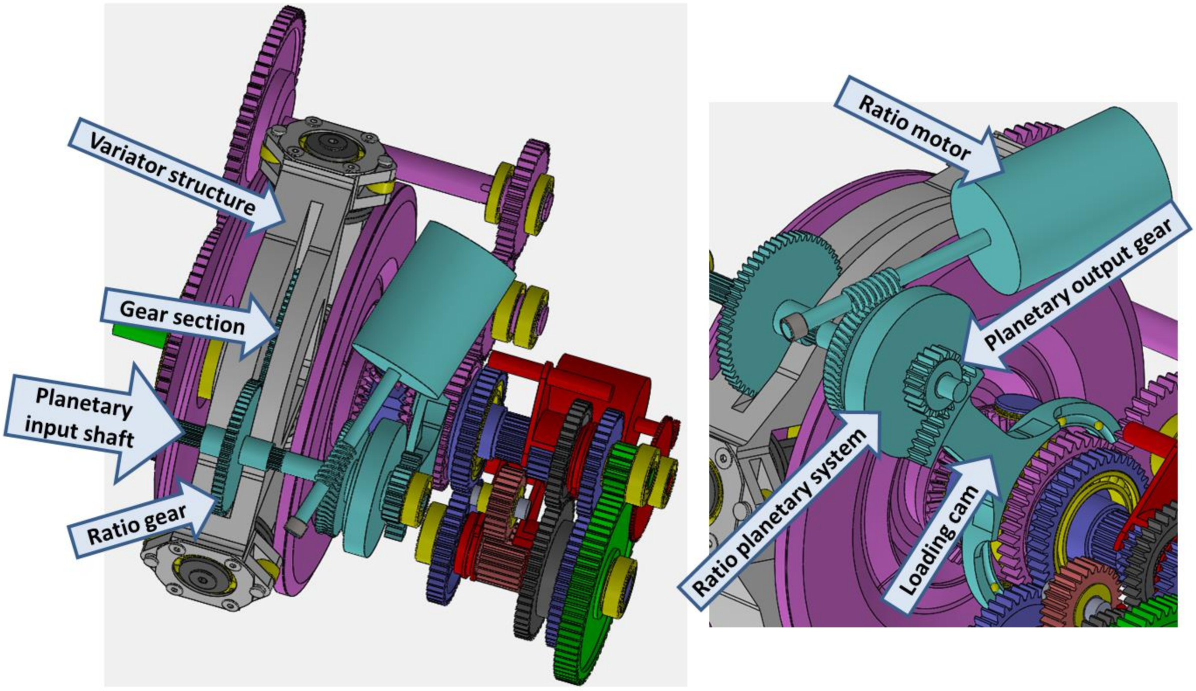

Figure 49 Ratio actuation and Loading cam

Therefore the torque on the Variator structure is a linear function of the clamping force and can therefore be used to actuate a loading cam to perform a portion of the clamping force.

(If clamping force is to be optimised to the full, a mechanism would be required to compensate for the variation of the traction coefficient through the ratio range.)

Figure 49 presents a system that performs both the ratio adjustment as well as serve as a loading cam mechanism. A Gear section is attached to the Variator structure and meshes and drives a Ratio gear.

The Ratio gear internal bore is splined and mates axially slidable with the Planetary input shaft which is also splined. The Planetary output gear is engaged with the teeth on the arm extension of the Loading cam.

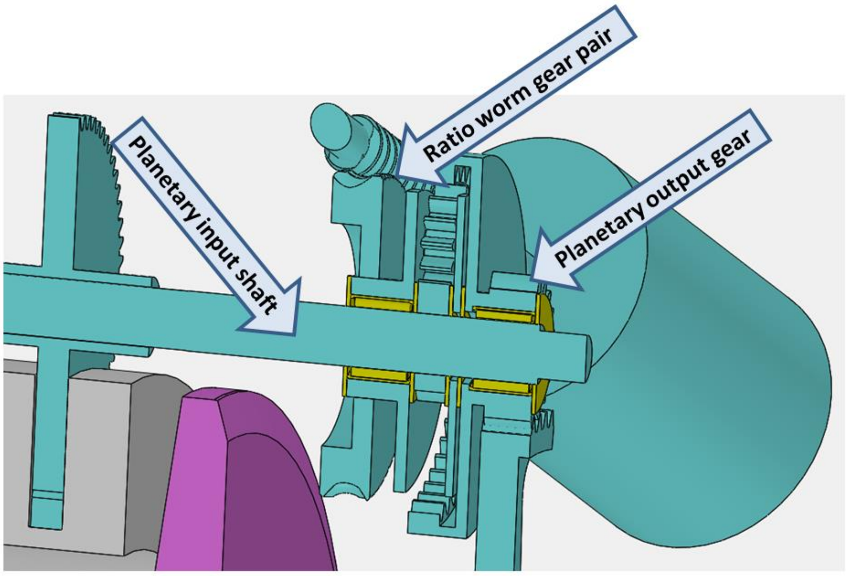

Figure 50 Ratio planetary system cross section view

Figure 50 shows that the Planetary input shaft is coupled to the sun gear of the Ratio planetary system, the Planetary output gear is coupled to the Ratio planetary system ring gear and the Ratio worm gear pair is coupled to the Ratio planetary system cage.

A position controlled Ratio motor drives the Ratio worm gear pair.

The Loading cam, as presented in Figure 51, on the one side includes Loading cam ramps, which mate with complementary ramps on the rear of the Clamping unit (see Figure 52), while on the other side the Loading cam includes a groove with ball bearings (yellow), with the ball bearings running in a complementary groove in the E^2 transmission casing on the other side. The functioning of the Ratio actuation and Loading cam is therefore as follows.

The torque on the Variator structure is transmitted to the sun gear of the Ratio planetary system.

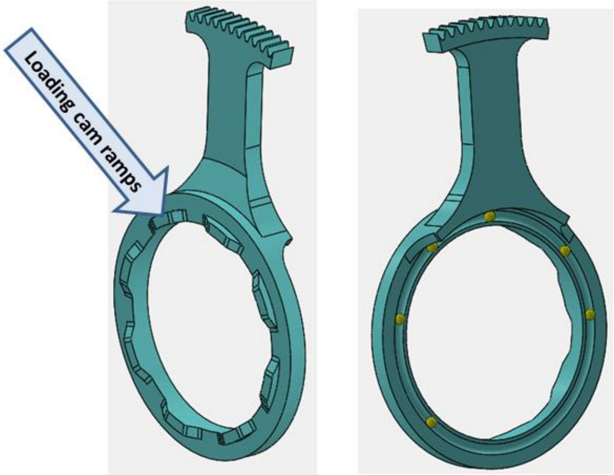

Figure 51 Loading cam

This torque creates a reaction toque on the planetary cage, which is held in place by the Ratio motors, as well as a reaction torque on the ring gear which is attached to the Planetary output gear.

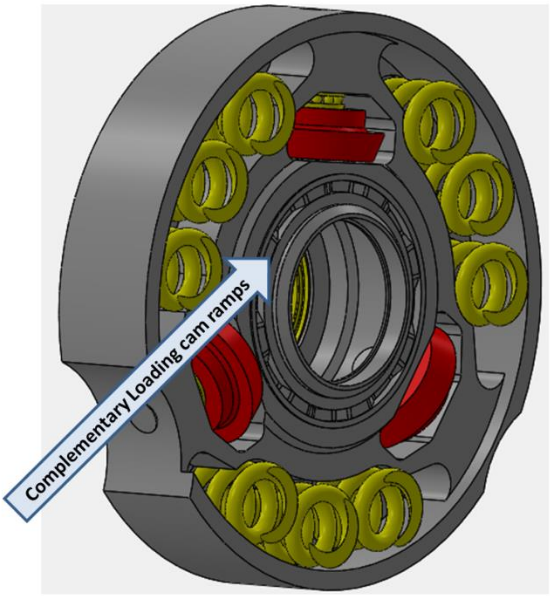

Figure 52 Clamping unit with ramps

The Planetary output gear creates a reaction torque on the Loading cam, while the Loading cam converts this reaction torque to a force via the Loading cam ramps. The reaction force on the mating ramps on the Clamping unit (see Figure 20 and Figure 52) serves as an additional clamping force to be added to the clamping force created by the mechanical springs. See section 6 for details on the Clamping unit design and purpose.

Note that the rotational displacement on the Loading cam to create the clamping force is negligible (it is only as a result of component stiffness's and tolerance gaps) and that the Loading cam operates equally under power transmission through the RADIALcvt in both directions (power source to wheels in normal driving and wheels to power source in for example engine braking).

By operating the Ratio motor, the rotational position of the Variator structure is changed and therefore also the RADIALcvt ratio as fully explained in (Naude, 2017).

Note that a non-linear relationship between the Variator structure torque and Loading cam ramp force can be created by implementing non-circular mating gears for the Gear section mating with the Ratio gear.

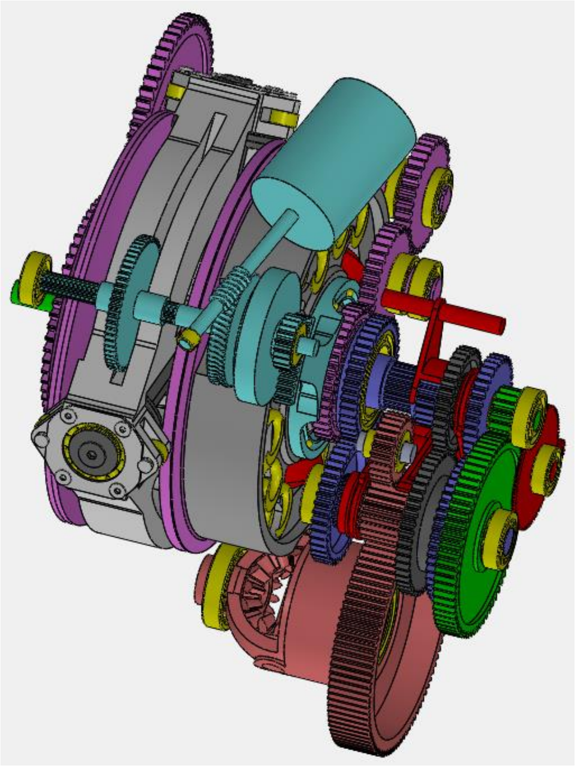

Figure 53 Complete E^2 transmission with casing hidden

Also note the various gear sizes and other parameters can be optimised to produce the required Variator torque to Loading cam clamping force conversion factor.

Figure 53 presents the complete E^2 transmission with a differential included (driven by the E2 output gear) with the casing hidden to serve as a front wheel drive transmission.

Figure 54 below presents the complete E^2 transmission with a 5 piece suitable casing.

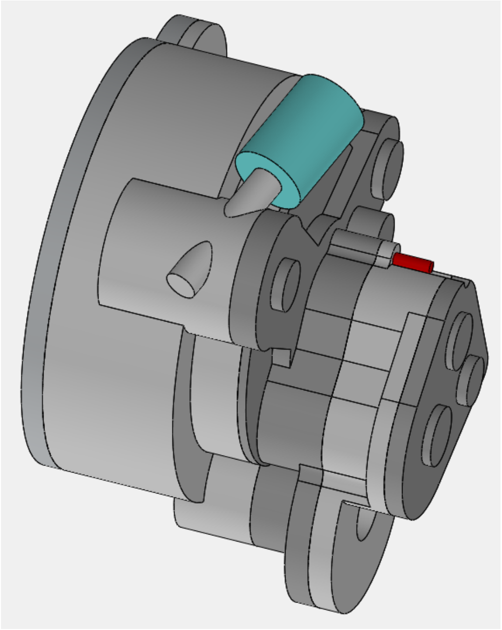

Figure 54 Complete E^2 transmission.

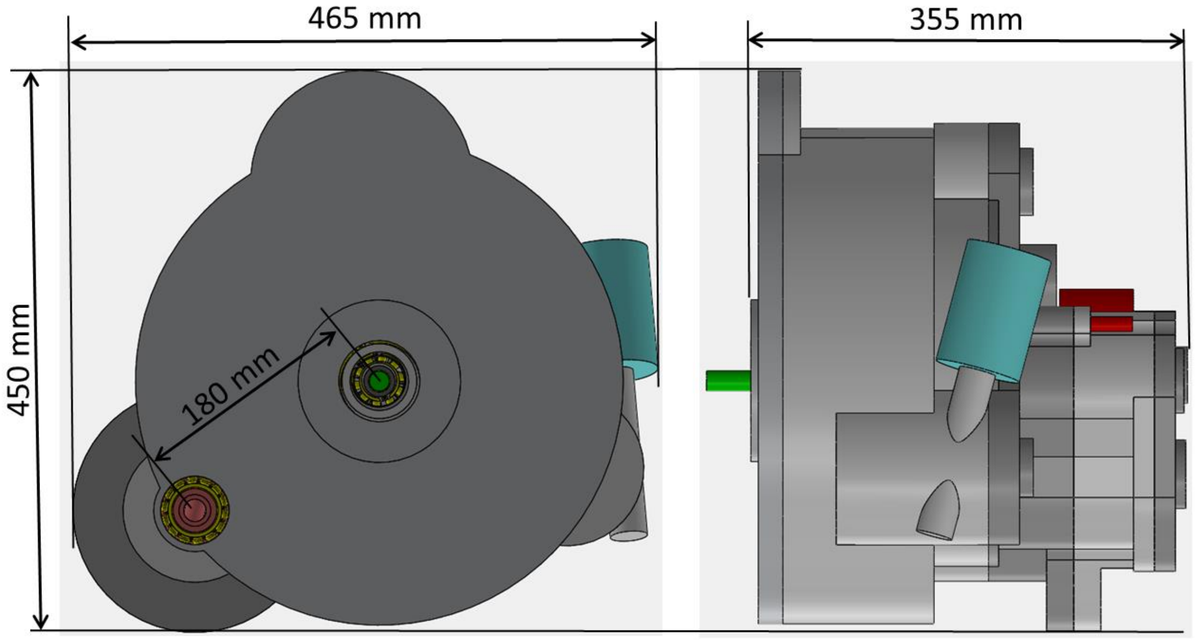

Figure 55 E^2 transmission dimensions

Figure 55 presents the general dimensions of the E^2 transmission, which is only given as an example and not optimised at all. This E^2 transmission should be able to handle in the order of 225 N.m input torque in all its ratios, as presented in section 4.3.4.

Note that this current section presented a configuration that does not include the RADIALcvt variator in a planetary loop configuration. This can easily be done, similar to that described in (McIndoe G. V., 2016) Figure 2, but the down side of such planetary loop is circulating power which effectively reduces the variator efficiency. However, with the already very high predicted mechanical efficiency such a planetary loop, with two modes might prove to be a commercial option considering all commercial factors. Such a planetary loop configuration also results in a two mode transmission in which the variator does not change its ratio when a mode shift takes place.

10 EV (Electric Vehicle) and geared motor RADIALcvt

In the previous designs above, the front Concave disk drive to the Combining planetary system was taken on the outside of the disks near its outer rim. The design presented in Figure 56 has a coupling between the front Concave disk and Combining planetary system via a shaft through the centre of the Convex and Concave disks. This design is typically suitable to be driven by an electric motor, which shaft is typically integrated with the RADIALcvt input shaft in Figure 56 and is therefore coupled directly to the RADIALcvt. This RADIALcvt configuration is typically suitable for industrial geared motor applications or electric vehicle applications and is referred to as the E RADIALcvt. Ratio control is done via a rotational position controlled power source, not shown.

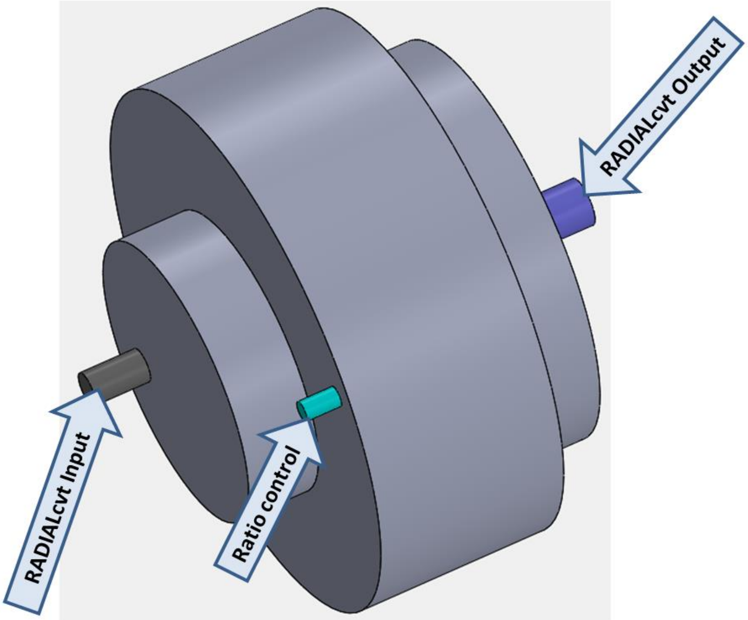

Figure 56 EV and geared motor RADIALcvt

Figure 57 presents the E RADIALcvt with its casing as well as the Clamping unit hidden, while Figure 58 presents a sectional view of the E RADIALcvt. The gear on the RADIALcvt input drives the Input gear which is splined and axially slidable on a hollow shaft that drives the Radial shafts and drivers, similar to that in the E^2 transmission. A gear on the Concave disk drives the Concave disk transfer shaft, in the opposite direction than that of the Concave disk, via an idler gear configuration, driving a gear on the Concave disk transfer shaft, see on the right of Figure 58.

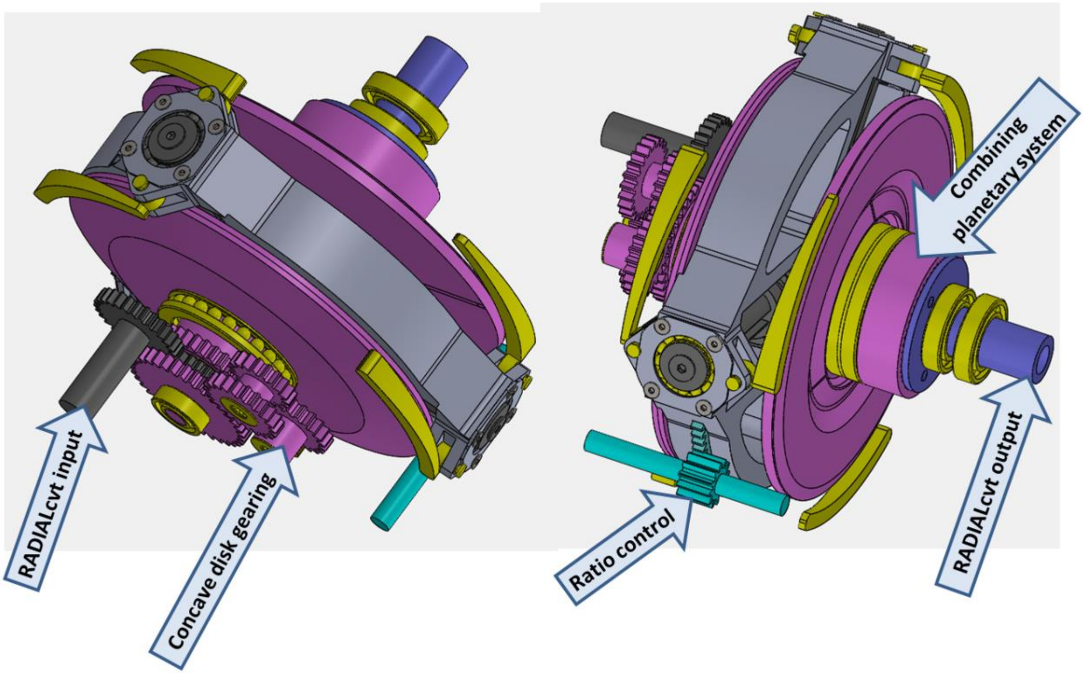

Figure 57 E RADIALcvt with casing and Clamping unit hidden

On the other end the Concave disk transfer shaft includes the sun gear of the Combining planetary system. This power path is shown in magenta colour. The Convex disk is attached to the ring gear of the Combining planetary system. This specific Combining planetary system has 3 planet gears. The cage of the Combining planetary system serves as the RADIALcvt output.

Note that the Combining planetary system and idler gear configuration gears and other meshing gear sizes, can be optimised to provide a torque split between the Convex disk and Concave disk other that a 50/50 split to account for the lower torque capacity of the Concave disk as presented in section 4. Planetary gear calculations can typically be done using (Shingley & Miscke, 1989).

Ratio control in the E RADIALcvt includes a gear on the Ratio control shaft meshing with a semi-circle gear attached to the Variator structure, shown in cyan colour.

The remainder of the components function in a similar way as presented in the E^2 transmission in section 9.

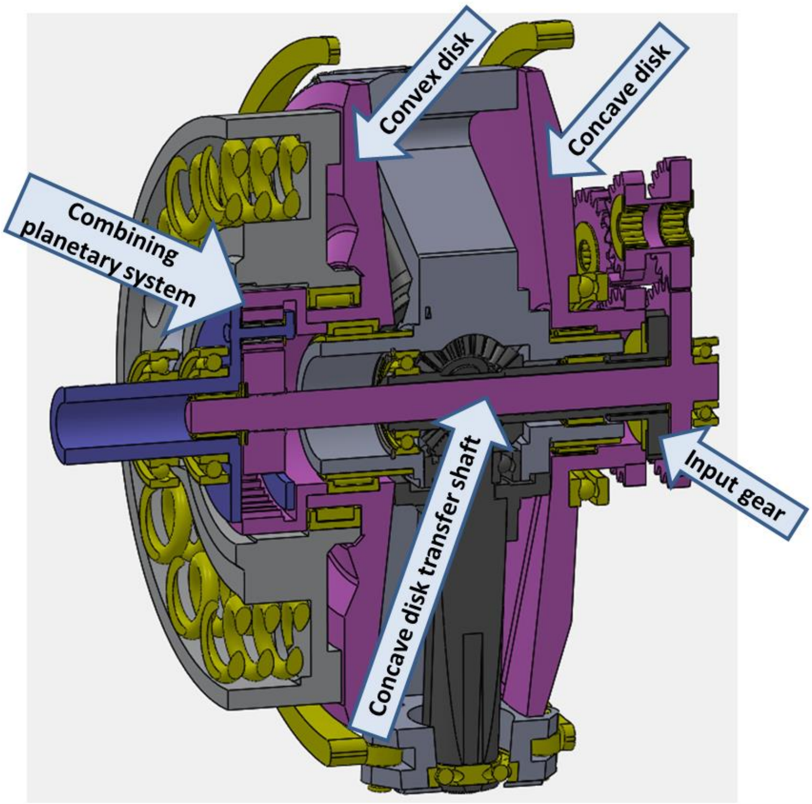

Figure 58 Sectional view of E RADIALcvt

Note that the configuration used in the E RADIALcvt can also be implemented in the E^2 transmission.

11 Published traction drive efficiencies and comparisons

11.1 Automotive

In automotive applications, CVT efficiencies have improved and have reached fuel efficiencies that are comparable to those of a manual transmission in certain driving cycles and conditions. In general, the emphasis on CVT's, are currently focussed on the fuel consumption advantages as a result of CVT capability as well as the advantages in harvesting energy from regenerative braking. However the mechanical efficiency of CVT's still lack behind that of manuals, DCT's and AT's. As AT's and DCT's increase their ratios (currently up to 10) to "approach" CVT capability their cost and complexity increases in direct competition with CVT's. With above in mind it is very difficult to find the actual mechanical efficiency of a complete commercial CVT broken down in terms of variator traction losses, clamping force bearing losses and hydraulic control losses. Technical research papers typically only give variator traction mechanical efficiencies or show % improvements on previous results.

Figure 59 represents a comparison of 2 pedal solutions published by Nissan at a VDI conference in 2016.

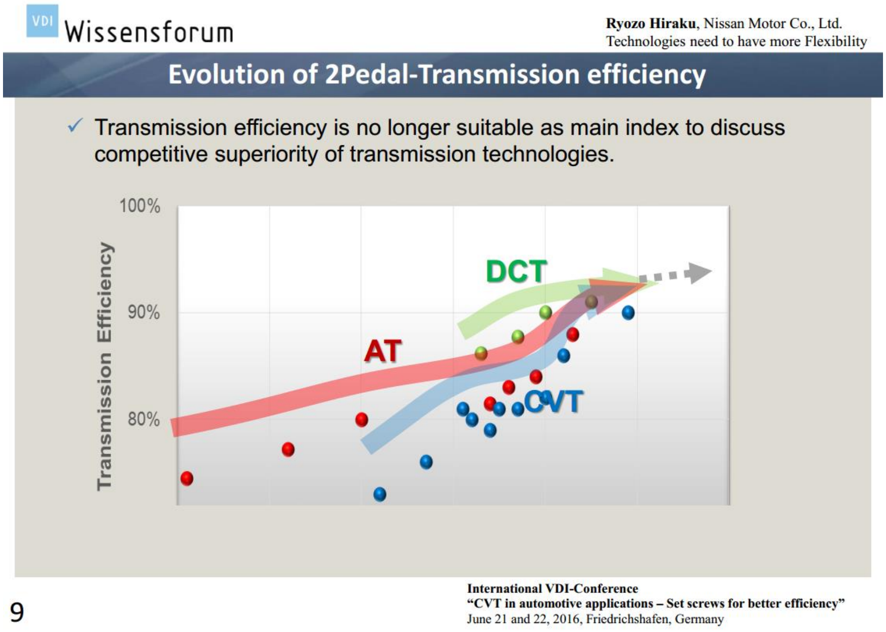

Wissensforum

Ryozo Hiraku, Nissan Motor Co., Ltd.
Technologies need to have more Flexibility

Evolution of 2Pedal-Transmission efficiency

✓ Transmission efficiency is no longer suitable as main index to discuss competitive superiority of transmission technologies.

International VDI-Conference
"CVT in automotive applications – Set screws for better efficiency"
June 21 and 22, 2016, Friedrichshafen, Germany

9

Figure 59 Comparison of the efficiency of 2 pedal solutions (Ryozo Hiraku, 2016)

Some general comparative power losses are given in (THE NATIONAL ACADEMIES PRESS, 2015). Figures 5.26 and Figure 5.27 of above are reproduced in Figure 60 below.

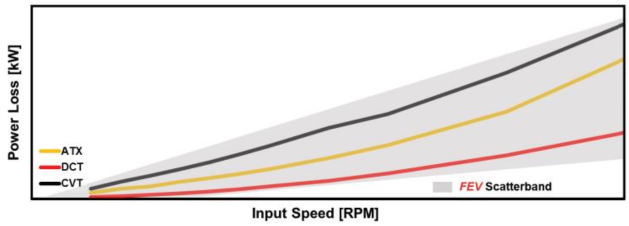

FIGURE 5.26 Transmission power losses as a function of input speed.
SOURCE: Govindswamy, Baillie, and D'Anna (2013).

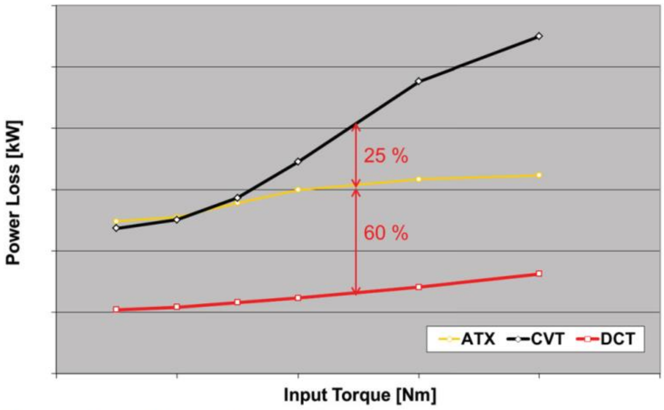

FIGURE 5.27 Transmission power losses as a function of input torque.
SOURCE: Baillie et al. (2014).

Figure 60 General transmission power loss comparisons (THE NATIONAL ACADEMIES PRESS, 2015)

Figure 61 presents the work of (Oswald Friedmann, 2002) and shows the huge disadvantage of CVT efficiency at low speed which also represents partial load conditions.

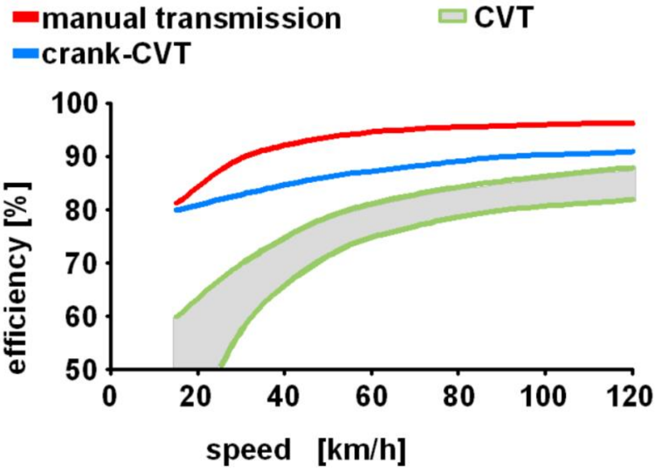

Fig. 11: *Efficiency Comparison*

Figure 61 General efficiency status in 2002 (Oswald Friedmann, 2002)

11.1.1 VariGlide

Figure 62 presents the fuel consumption comparison between Dana's VariGlide (McIndoe, 2016) and a DCT. Dana claims a peak efficiency of 94.6% (McIndoe, 2016).

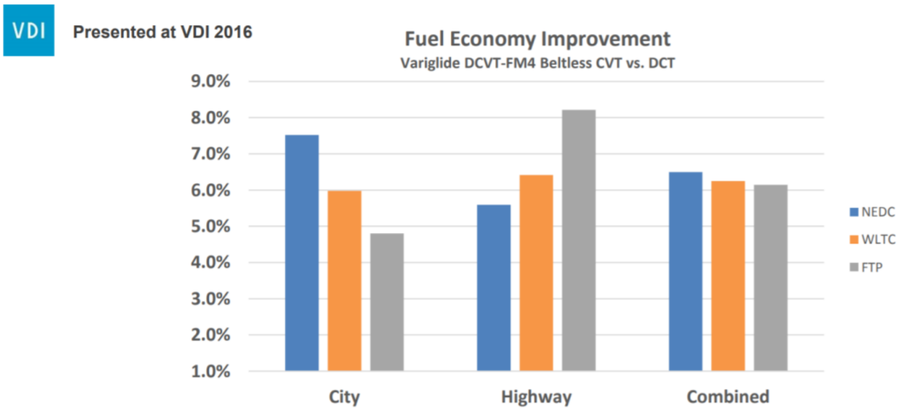

Figure 62 Dana's Variglide (McIndoe, 2016)

A comparison of a commercial multi-mode belt CVT vs a multi-mode VariGlide was performed by (McIndoe G. V., 2016). Figure 63 present the transmission efficiency of the two mode belt CVT vs a two mode VariGlide while Figure 64 the two mode belt CVT vs a three mode VariGlide. The blue lines represent the VariGlide efficiency.

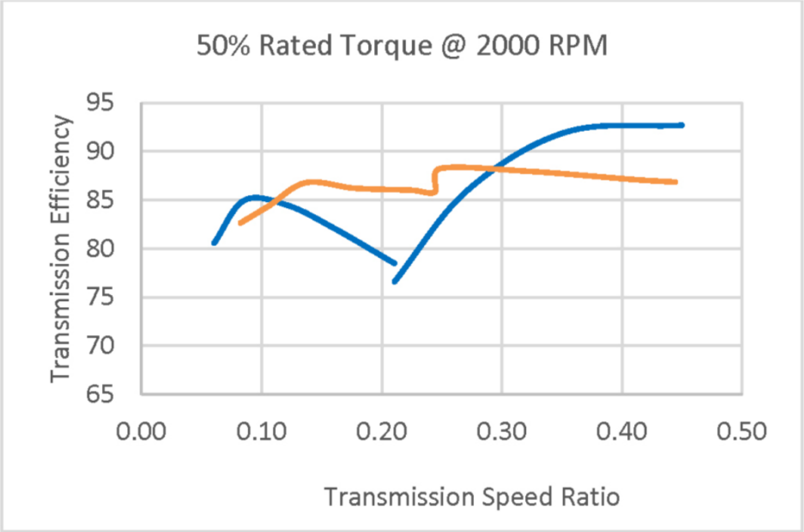

Figure 11. Comparison of Over All Transmission Efficiency.

Figure 63 Two mode belt CVT vs a two mode VariGlide (McIndoe G. V., 2016)

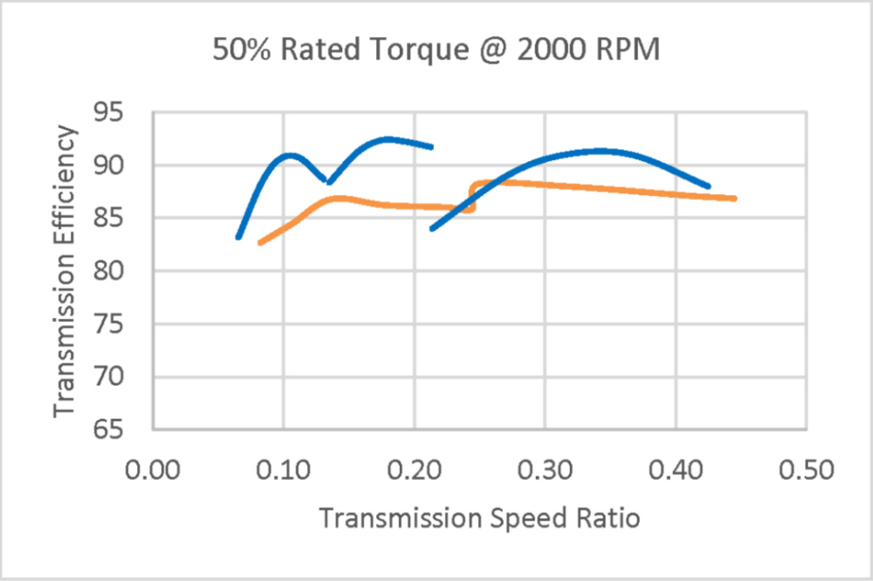

Figure 12. Next Generation Multi Mode VariGlide VG-CVT Compared to the Production CVT.

Figure 64 two mode belt CVT vs a three mode VariGlide (McIndoe G. V., 2016)

Figure 65 presents a breakdown of the losses as presented by (McIndoe G. V., 2016) without a vertical scale. However noting that the highest recorded multimode VariGlide transmission efficiency was given as 92% (McIndoe G. V., 2016), the scale can be estimated as around 8% for the two right hand columns or roughly 2% per increment as superimposed on Figure 65.

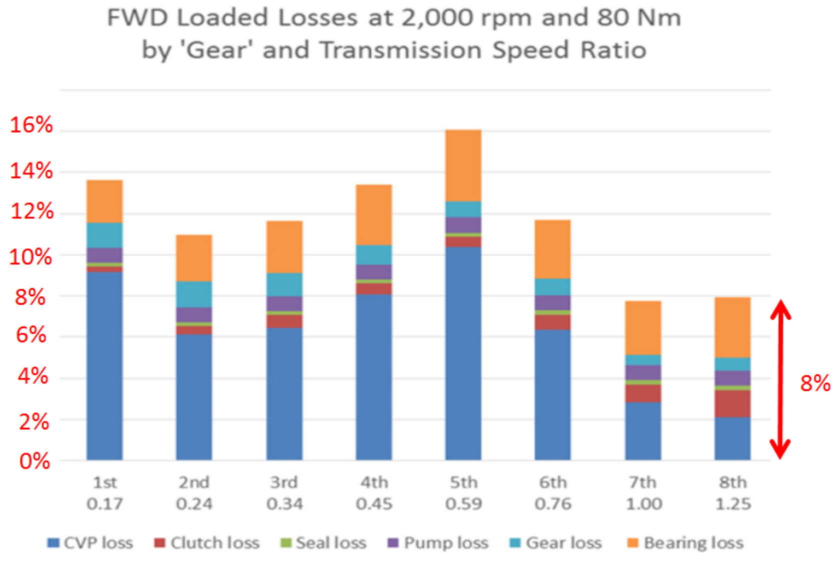

Figure 5. VariGlide Multimode Transmission Losses

Figure 65 VariGlide loss breakdown (McIndoe G. V., 2016) with estimated vertical scale superimposed.

11.2 Non-automotive

Below are some published efficiencies on non-automotive commercial CVT's. Note that it is in some cases not stated at what load percentage below efficiencies were measured but it can be assumed it is at high load percentages.

11.2.1 CVTCorp

CVTCORP manufactures a toroidal CVT for applications in the agricultural, off-highway and industrial markets. Figure 66 below represents their variator efficiency as published on their website.

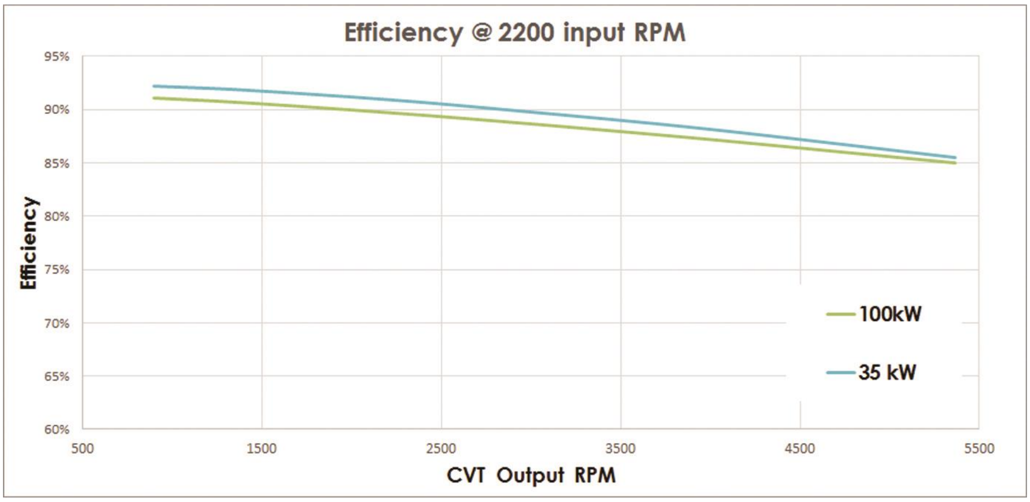

Figure 66 CVTCORP variator efficiency (Technology, 2017)

11.2.2 Kopp variator

Allspeeds manufactures a planet ball/cone variator for the industrial market. Figure 67 below represents their planet ball based variator efficiency as published on their website.

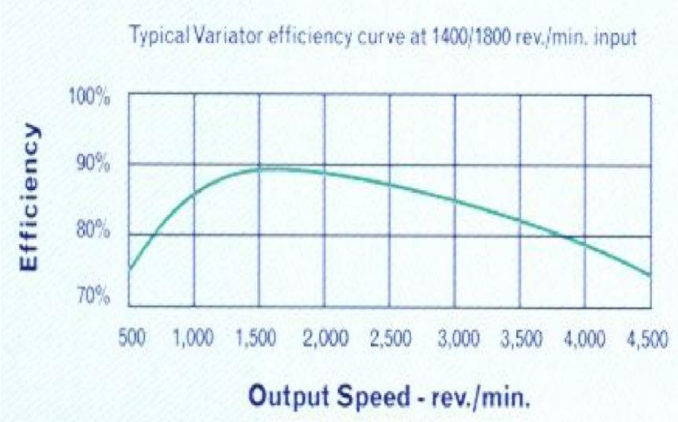

Figure 67 Kopp variator efficiency (Allspeeds Speed Control, 2017)

11.2.3 Darali variator

Figure 68 present the efficiency of the Darali Disco variator, a planet disc type variator, as published on their website. This variator has a ratio range of 6.

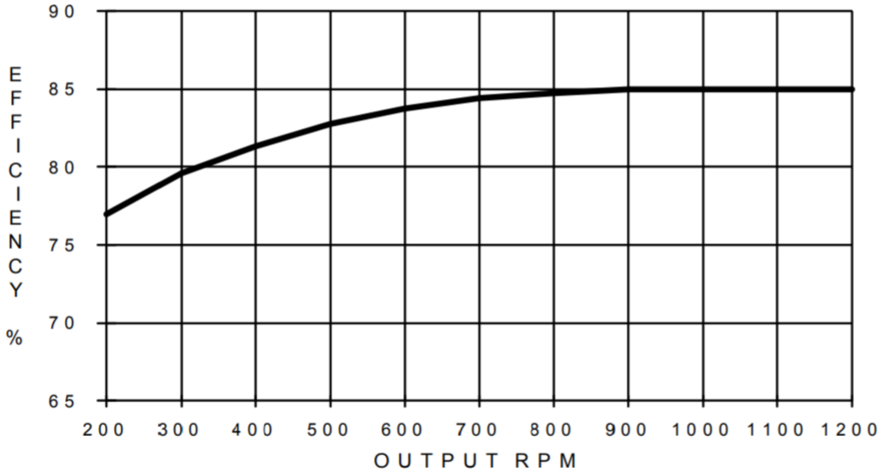

Figure 68 Darali Disco Variator efficiency (Darali)

Note than both the Kopp and Darali variators maximum input torque specifications vary as the ratio varies.

11.2.4 Turbo Trac

Figure 69 presents the efficiency result obtained by Turbo Trac Inc. in 2004 on a variator intended for trucks.

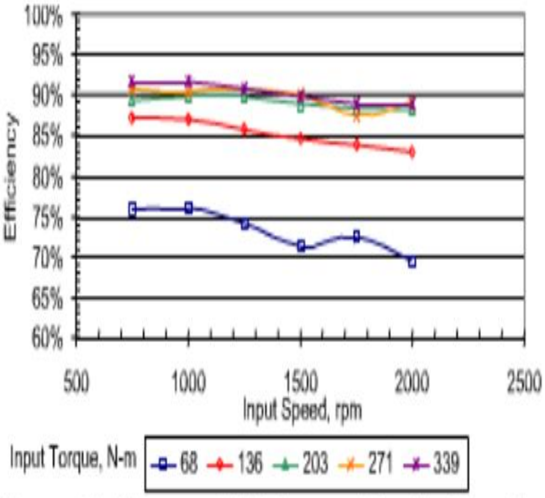

Figure 12: Measured Efficiency of the Variator Alone on the SwRI Test Stand Operating at a Speed Ratio (ω_{in}/ω_d) of 0.6

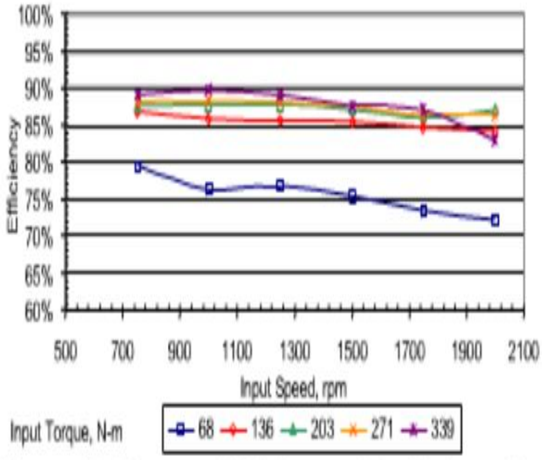

Figure 13: Measured Efficiency of the Variator Alone on the SwRI Test Stand Operating at a Speed Ratio (ω_{in}/ω_d) of 1.0

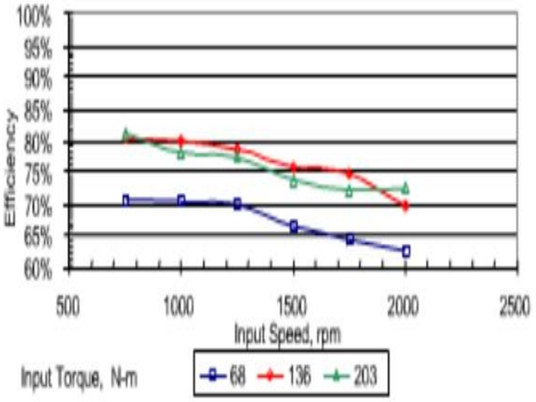

Figure 14: Measured Efficiency of the Variator Alone on the SwRI Test Stand Operating at a Speed Ratio (ω_{in}/ω_d) of 2.0

Figure 69 Turbo Trac variator efficiency (Carter, Pohl, Raney, & Sadler, 2004)

12 References

Allspeeds Speed Control. (2017, 09 04). Retrieved 09 04, 2017, from Allspeeds: http://www.allspeeds.co.uk/wp-content/files_mf/brochure.pdf

Carter, J., Pohl, B., Raney, R., & Sadler, B. (2004). The Turbo Trac Traction Drive CVT. *SAE International*, 7.

Darali. (n.d.). *DARALI® Disco Variators Design Features.* Retrieved 09 28, 2017, from DARALI Cycloidal speed reducers: http://www.darali.com/disco/page4.pdf

Heumann, H., Briffet, G., & Burke, M. (2003). *System efficiency optimisation of the Torotrak Infinitely Variable Transmission (IVT).* Lancashire, UK.: Torotrak Development.

Jans, C. (2005). *Slip measurement and control in a cone ring transmission.* Eindhoven: Eindhoven University of Technology.

Leimei, L. (2013). *Assesment of Effects of Surface Roughness and Oil Viscosity on Friction Coefficient under Lubricated Rolling-sliding Conditions.* Komatsu.

Lichao, P. (2013). *Tribology of a CVT traction drive.* Eindhoven: Eindhoven University of Technology.

Loewenthal, S. H., & Rohn, D. A. (1983). *Regression analysis of traction characteristics of two traction fluids.* Cleveland, Ohio: NASA Technical paper 2154.

Loewenthal, S. H., & Zaretsky, E. V. (1985). *Design of Traction Drives.* Ohio: NASA Reference Publication 1154.

Loewenthal, S., & Rohn, D. (1983). Traction Behavior of Two Traction Lubricants. *American Society of Lubrication Engineers.* Houston, texas.

McIndoe, G. (2016). Variglide Beltless CVT. *VDI.*

McIndoe, G. V. (2016). Effciency Analysis of Multi-Mode Passenger Car Transmission. *SAE Technical Paper 2016-01-1108*.

Naude, J. (2017, 08 04). *Patent No. WO2017/143363.* PCT.

Oswald Friedmann, W. H. (2002). The Crank-CVTMore economical than a manual transmission and more comfortable than a conventional CVT? *LUK Symposium 2002* (pp. 107-116). Germany: Schaeffler.

Ryozo Hiraku. (2016). Technologies need to have more Flexibility. *CVT in automotive applications - Set screws for better efficiency.* Friedrichshafen: International VDI-Conference.

Shingley, J., & Miscke, C. (1989). *Mechanical Engineering Design* (Fifth ed.). Singapore: McGraw-Hill.

SKF. (1989). *SKF General catalogue.* Germany.

SKF. (n.d.). *SKF.* Retrieved 8 4, 2017, from SKF Bearing calculator: http://webtools3.skf.com/BearingCalc/selectProduct.action

Technology. (2017, 09 04). Retrieved 09 04, 2017, from CVTCORP: http://www.cvtcorp.com/en/technology

THE NATIONAL ACADEMIES PRESS. (2015). *Cost, Effectiveness, and Deployment of Fuel Economy Technologies for Light-Duty Vehicles.* Washington, DC, USA: THE NATIONAL ACADEMIES PRESS.

TIMKEN. (2017). *TIMKEN product catalog A21.*